



Phase-field modeling of carbon fiber oxidation coupled with heat conduction

Marina Sessim, Linyuan Shi, Simon R. Phillpot, Michael R. Tonks*

Department of Materials Science and Engineering, University of Florida, Gainesville, 32611, FL, USA

ARTICLE INFO

Dataset link: <https://github.com/tonkmr/macaw>

Keywords:

Phase-field
MOOSE framework
Carbon oxidation
PICA
Macaw

ABSTRACT

In this paper, we developed a multiphysics mesoscale model of carbon fiber oxidation in the upper most layer of a phenolic impregnated carbon ablator thermal protection system. The presented model uses the phase-field method to capture the reduction of carbon fibers due to an oxidation reaction between carbon and oxygen to form carbon monoxide. The model is fully coupled with heat transport in the system, including the heat absorbed by the endothermic oxidation reaction. We implemented the model in the new Macaw application, created using the Multiphysics Object-Oriented Simulation Environment (MOOSE). The model was verified against an analytical solution of surface reactions. A sensitivity analysis revealed that the parameters that most impact the oxidation time are those related to the reaction rate. The model was demonstrated using 2D and 3D simulations of the oxidation of multiple fibers, illustrating the impact of fiber diameter, temperature, and gas flow on the fiber oxidation.

1. Introduction

The Thermal Protection System (TPS) is a combination of materials and components that shields a spacecraft during an atmospheric entry. It has the fundamental role of insulating the structural components and payload. The Phenolic Impregnated Carbon Ablator (PICA) is NASA's heritage ablative TPS [1,2]. Ablative TPS are more robust and withstand higher entry velocities than reusable TPS, such as the ones used in the Space Shuttle program [3]. PICA is a light weight polymeric ablative material that consists of a structure of carbon fibers impregnated with a phenolic resin. The carbonaceous structure yields high atmospheric erosion resistance, also referred to as ablation resistance [1]. The phenolic resin decomposes under the high temperatures experienced during the atmospheric entry through pyrolysis, an endothermic process that is crucial for insulation [4]. PICA is successful due to its combination of low density, good ablation resistance, and good insulating properties [1,5]. The Stardust capsule, part of NASA's Discovery mission, successfully entered Earth's atmosphere with a PICA TPS at a velocity of 12.9 km/s and experienced a peak heat flux of 1100 W/cm² [2]. The analysis of the Stardust post-flight data revealed that PICA performed well; its measured recession depth was 25%–61% lower than predicted [2]. The discrepancy between the prediction and the actual flight data demonstrates that there is a need to improve and develop more accurate prediction codes that could be used to reduce overdesign and reduce weight.

FiberForm[®] (Fiber Materials, Inc., Biddenford, ME, USA) is the carbon-fiber structure of the heritage PICA. The fibers are loosely

packed, giving the structure a 85%–91% porosity [6]. They have a diameter of 5–6 μm and are bundled in strands of five to six fibers. The strands are dispersed in the plane perpendicular to the through-thickness direction of the TPS and bonded together by an organic binder that is transformed into a carbonaceous char during the manufacturing process [7]. The phenolic resin is then impregnated into the carbon-fiber structure to create the final PICA. The PICA microstructure and properties vary due to the manufacturing process and discrepancies in the raw materials [8,9].

The structure of the carbon fibers directly impacts their properties. A carbon fiber is composed of multiple layers of graphitic sheets folded around a center axis [10–12]. Along the basal plane of graphite, the carbon atoms are linked by strong covalent bonds and the thermal conductivity is very high, on the order of 100 to 1000 W/(m K) for a perfect structure at room temperature [13–16]. Hence, the thermal conductivity of the fiber itself increases with an increasing average size of the graphitic sheets [11,17,18]. The sheets are connected by weak Van der Waals forces, which is an obstacle for heat conduction. The thermal conductivity through the layers decreases with increasing interlayer spacing between the basal planes [17]. The values of the thermal conductivity in the through-interlayer direction are two to three orders of magnitude lower than in the basal plane [13]. The placement of these fibers in the substrate of PICA is strategic to diffuse the heat parallel to the surface of the TPS and insulate in the through-thickness direction. The perfect graphite structure is resistant to oxidation, but the edges are much more susceptible [19,20]. Thus, fibers oxidize faster when

* Corresponding author.

E-mail address: michael.tonks@ufl.edu (M.R. Tonks).

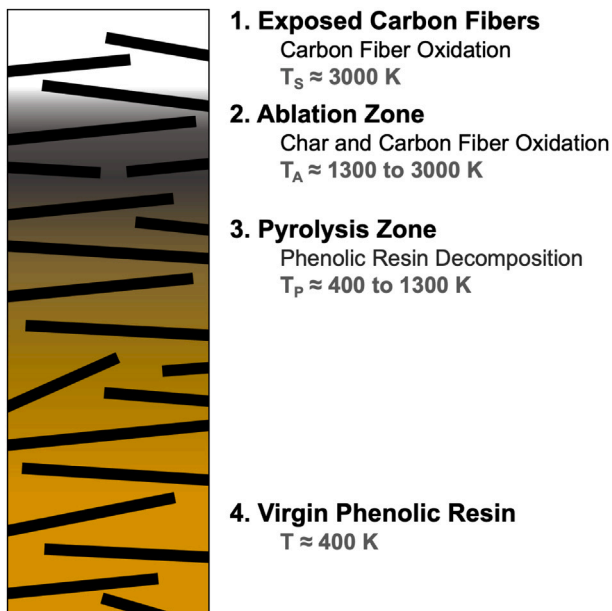


Fig. 1. Schematic of a cross-section of PICA TPS. The black rectangles represent carbon fibers, the yellow phase the phenolic resin, and the dark gray phase the char. Four different zones are shown, including the phenomena that occur and typical temperatures. This work focuses on the first zone.

more edges are exposed. The specific fiber structure is dependent on the precursor and manufacturing process used to create them [21]; heritage PICA FiberForm used a rayon-fiber precursor [22].

During atmospheric entry, the spacecraft experiences an intense heat flux; the TPS surface temperature may be as high as 3000 K [23–25], causing it to ablate. The Stardust post-flight analysis [2] greatly increased our understanding of how and where the ablation takes place in the TPS. The imaging of PICA post-flight revealed a top layer composed of mostly exposed carbon fibers, then a layer of carbon fibers and charred resin, a subsequent layer with partially pyrolyzed resin, and a bottom layer of virgin PICA [2]. Fig. 1 presents a schematic of the cross section of the PICA TPS after atmospheric entry, inspired by the observed regions in the Stardust analysis [2,25]. The indicated temperatures are an estimate based on previous flights, experiments, and computational data [2,4,25,26].

The ablation results from a combination of several physical and chemical processes that occur in the various layers. In the outermost layer, the dominant processes are spallation, when a section of the carbon structure breaks off due to a combination of mechanical and thermal stresses [3], sublimation, the direct change of solid to gaseous carbon, and oxidation, the loss of mass due to the reaction of oxygen with the surface of the carbon fibers and char to form gaseous products such as carbon monoxide (CO) and carbon dioxide (CO₂). Solid carbon oxidation is quite different from metal oxidation that produces a solid oxide and for which electric charge transport is a rate-limiting step. In solid carbon oxidation, the formation of gases such as CO and CO₂ are not significantly impacted by charge transport. In the second layer, commonly referred to as the ablation zone [25], both the charred resin and the carbon fiber oxidize. The porous char oxidizes and recedes faster, exposing the fibers. In the third layer, referred to as the pyrolysis zone, the phenolic resin is gradually transformed into char. This process is endothermic and produces gases that aid the thermal insulation of the TPS [4,27].

While both the pyrolysis of the resin and the oxidation of the char and fibers contribute to the ablation rate and the thermal protection, they occur at different temperatures at distinct regions within the PICA. Thus, mesoscale simulations that do not resolve the full thickness

of the TPS can target them separately. The oxidation of the carbon fibers has been the target of such mesoscale modeling, due to its relative simplicity compared to pyrolysis and the fact that it occurs at the outermost layer of the PICA. These models have used Monte Carlo (MC) methods that use a random walk technique to model the mass transfer and diffusion throughout the domain. When a gas particle reaches a carbon surface, a sticking probability defines if the reaction will occur. This methodology has been applied to model the steady-state and transient oxidation of carbon fibers in carbon/carbon composites [28–30]. Lachaud et al. [31] established a multiscale approach to include microstructural-level MC models in engineering-scale predictions. Nonetheless, no microscale model has been fully coupled with models of the heat transport.

It is important to understand the complex physical phenomena that result in the ablation of PICA material, because they directly determine the level of thermal protection it provides. In addition, these physical phenomena are tightly coupled; for example, the rate of the chemical reactions are highly sensitive to temperature and are endothermic, and thereby change the temperature. Also, the configuration of the fiber structures impact the flow of oxygen and heat, which also impacts the thermal protection. Thus, mesoscale simulations that account for these tightly coupled phenomena and resolve the fiber structures can provide precise descriptions of the performance and properties of the material. Calculating more precise values for the thermal properties of the PICA material and the correlation of these properties to the overall ablation rate will yield more accurate prediction of the PICA performance and will result in less over-design [31].

In this work, we present a novel mesoscale model that captures the tightly coupled heat transport and temperature-dependent oxidation of carbon fiber structures in the outermost layer of PICA during entry. It does not consider spallation. Our model is based on the phase-field method, which simulates diffusion-controlled microstructure evolution [32–34]. In the phase-field method, each microstructure feature is represented by a non-conserved variable field. The chemical species in the system are represented by conserved concentration variables, which follow a generalized diffusion equation. The variables are continuous throughout the domain and transition smoothly across the interface between different phases. The phase-field variables evolve to lower the overall free energy of the system. We developed an open-source mesoscale application for modeling ablation named Macaw [35]. Macaw solves coupled phase-field and heat transport equations using the finite element method and is based on the Multiphysics Object-Oriented Simulation Environment (MOOSE) [36, 37]. Therefore, the local temperature is computed simultaneously with the local concentrations and microstructure evolution. The chemical reaction kinetics from the oxidation process is incorporated in the phase-field method and is dependent on the local temperature.

This paper summarizes our model of the carbon fiber oxidation in the outermost layer of PICA and how it is implemented in Macaw. Section 2 details the phase-field carbon fiber oxidation model coupled with heat conduction. Section 3 presents multiple verification efforts used to determine the mathematical accuracy of the model. Section 4 presents a sensitivity analysis that evaluates the impact of the individual thermophysical properties and model parameters on the oxidation time of a single fiber. Section 5 demonstrates the oxidation behavior of multiple carbon fibers in 2D and 3D domains. We conclude in Section 6.

2. Model description

In this section, the methods and models that are an essential part of this work are discussed. First, the mathematical description of the phase-field method is presented. We also describe how the chemical reaction kinetics are incorporated in the model. The full coupling with heat conduction is explained, in addition to the incorporation of the energy of reaction. Later, the coupled implementation of the mathematical models using the MOOSE framework is described.

2.1. The phase-field model

Our phase-field model predicts the carbon fiber oxidation that occurs within the first layer of PICA material during atmospheric entry. The model represents two regions of material, the carbon fibers and the open volume filled with gas. It also represents chemical species, including carbon (C) atoms, oxygen (O) atoms, and CO molecules. In reality, additional reaction products can form, such as CO₂, but CO is the most common. So, for simplicity, we only include CO in the simulations. Each of these chemical species are represented with a continuous variable field that evolves with time according to a partial differential equation (PDE), to represent the loss of carbon fiber volume and the generation of CO. The reaction between C and O atoms to produce CO is represented using reaction terms in the PDEs that define the evolution of the chemical species. The fiber and gas regions and the chemical species evolve to minimize overall energy in the system. In this section, we first introduce the PDEs that define the evolution of the two regions and the three chemical species. Then, we describe the models used to describe the free energy of the fiber and gaseous regions.

2.1.1. Phase-field PDEs

The phase-field method has advanced over the past couple of decades to become a powerful tool to model microstructure evolution for many different applications. For a general description and overview of the method, we recommend the following review articles: [32–34]. In our phase-field model of carbon fiber oxidation, we employ a non-conserved variable field to describe the carbon fibers η_f and another to describe the gaseous region η_g . $\eta_f = 1$ and $\eta_g = 0$ in the fibers and $\eta_f = 0$ and $\eta_g = 1$ in the gaseous region; they both smoothly transition between these values over the fiber surface, assuming a profile similar to a hyperbolic tangent function [38,39]. This results in all surfaces having a finite thickness. The multiple order parameter formulation will facilitate the addition of other phases to the model in the future, such as the char. The number density of C, O, and CO are represented by their atomic fractions x_O , x_C , and x_{CO} , respectively.

For our oxidation model, we use the grand-potential model (GPM) that was first proposed by Plapp [40]. It is based on the minimization of a grand-potential functional Ω . In the GPM, the bulk and interfacial free energies are decoupled and the independent variables describing the chemical species are the chemical potentials instead of the atomic fractions. It maintains the chemical potential equilibrium across the interfaces and enables independent control over the interface energy and its diffuse thickness. The GPM has been used to model a wide range of physical phenomena, including fission gas bubble evolution, sintering, and multiphase materials with mismatch strains between phases [39,41,42].

In the GPM, each chemical species follows a generalized diffusion equation of the form [40]

$$\frac{\partial \rho_i}{\partial t} = \nabla \cdot M_i \nabla \frac{\delta F}{\delta \rho_i}, \quad (1)$$

where ρ_i is the number density of species i , with $i = C, O,$ or CO , in units of atom/m³, M_i is the atomic mobility in units of atom²/(J m s), and F is the free energy functional in units of J/m³. The number density can be written as

$$\rho_i = \frac{x_i}{V_a}, \quad (2)$$

where x_i is the atomic fraction of species i (unitless) and V_a is the atomic volume in units of m³/atom. The chemical potential of species i

$$\mu_i = \frac{\delta F}{\delta \rho_i}, \quad (3)$$

and it has units of J/atom. The number density and the chemical potential are related through the free energy densities of each phase. The

free energies are later converted to grand-potential densities, and the total grand-potential of the system is interpolated between each phase. Eq. (3) is used to obtain the species number density in each phase, and the number density in the system is also interpolated between each phase.

The total grand-potential of the system is derived from the cumulative energy contributions from the bulk of the material and the interfaces between phases

$$\Omega = \int_V (\omega_{chem} + \omega_{inter} + \omega_{grad}) dV, \quad (4)$$

where ω_{chem} is the bulk grand-potential density and ω_{inter} combined with ω_{grad} represent the grand-potential density associated with free surfaces in the system. The grand-potential densities have units of J/m³. We use the multiphase interfacial grand-potential density function

$$\omega_{inter} = m \left(\sum_{\alpha} \left(\frac{\eta_{\alpha}^4}{4} - \frac{\eta_{\alpha}^2}{2} \right) + \frac{3}{2} \eta_f^2 \eta_g^2 + \frac{1}{4} \right), \quad (5)$$

where m is a constant with units of J/m³ and we sum over the two phases in the system [38,39]. The gradient grand-potential density is

$$\omega_{grad} = \frac{\kappa}{2} \sum_{\alpha} |\nabla \eta_{\alpha}|^2, \quad (6)$$

where κ is a model parameter with units of J/m. The values of m and κ are functions of the surface energy of a carbon fiber [38,39]

$$m = 6 \frac{\sigma_{int}}{\delta_{int}} \quad (7)$$

$$\kappa = \frac{3}{4} \sigma_{int} \delta_{int}, \quad (8)$$

where σ_{int} is the surface energy in J/m² and δ_{int} is the characteristic interface width in m. δ_{int} is a model parameter that is selected to be as small as possible, without making the computational cost too high (since the element size must be several times smaller than δ_{int}).

The chemical grand-potential density of phase α (where $\alpha = f$ or g) is derived from the corresponding free energy density f^{α} through a Legendre transformation [39,40], i.e.

$$\omega^{\alpha} = f^{\alpha} - \sum_i \mu_i \rho_i, \quad (9)$$

where we sum over the three chemical species in the system (C, O, and CO). In order to calculate the total grand-potential density of the system, we use a continuous multiphase interpolation function developed by Moelans [43]

$$h_{\alpha} = \frac{\eta_{\alpha}^2}{\eta_f^2 + \eta_g^2}, \quad (10)$$

where $\alpha = f$ or g . Material property values are interpolated across the interface by this interpolation function and are constant inside each phase. The total bulk grand-potential density of the system is

$$\omega_{chem} = h_f \omega^f + h_g \omega^g. \quad (11)$$

The evolution of the variables describing the fiber and gaseous regions is defined by an Allen–Cahn equation of the form [44]

$$\frac{\partial \eta_{\alpha}}{\partial t} = -L \frac{\delta \Omega}{\delta \eta_{\alpha}}, \quad (12)$$

where L is the phase mobility with units of m³/(J s). The phase mobility controls the rate of change of the order parameters. It is related to the surface mobility and width according to [38]

$$L = \frac{4}{3} \frac{M_{surf}}{\delta_{int}}, \quad (13)$$

where M_{surf} is the surface mobility in units of m⁴/(J s) and describes the rate at which the surface of the fiber restructures as carbon atoms react with oxygen atoms. In this work, we assume that this mobility is

very fast, such that the shrinkage rate of the carbon fibers is controlled by the reaction rate constant not by the surface mobility. Therefore, the mobility is proportional to the reaction rate constant K :

$$M_{int} = aK, \quad (14)$$

where a is the proportionality constant. We performed a parametric study to evaluate the parameter space of a and its implications on the phase-field results. In the study, we evaluated a series of phase mobility values in our phase-field oxidation model at a constant temperature, and calculated the final oxidation time for a single carbon fiber. We found that a value of $a = 9.6 \times 10^3$ m/(atom J) was large enough to ensure that the oxidation rate was governed by the reaction rate constant. Since the reaction rate constant is a function of the local temperature, which can vary across the interfaces, we use the average temperature in the fiber to determine its value.

2.1.2. Free energy expressions

For our phase-field model of oxidation, we need to define functions that describe the free energy density of the fiber and gas phases. As described previously, carbon fibers are composed of graphitic sheets folded around the center axis. For the free energy we approximate the carbon fiber structure as a single crystal lattice of carbon atoms with a known atomic volume (estimated from the fiber density), where each lattice site is occupied by either C atoms or is vacant. Thus, the atom fraction of vacancies in the fiber phase is

$$x_v = 1 - x_C. \quad (15)$$

The gaseous species O and CO have a high formation energy in a carbon fiber, have very low diffusion coefficients (see [45,46] for diffusion behavior in a similar graphitic structure), and are much more likely to chemically react on the surface than to diffuse into the bulk of the fiber. Thus, we assume that O and CO concentrations within carbon fibers are extremely low. We also assume that the vacancy concentration within the fiber structure is small. Thus, we employ the dilute-limit approximation of the ideal solution model, which is referred to in this paper as the dilute solution model, for the free energy density of the solid carbon fiber phase:

$$f^f = f_{min}^f + \sum_i \frac{E_i^f}{V_a} x_i + \frac{k_B T}{V_a} [x_i \ln(x_i) - x_i], \quad (16)$$

where k_B is the Boltzmann constant, E_i^f is the species i formation energy, and we sum over the three dilute species (O, CO, and vacancies). We then use Eq. (15) to make the free energy density a function of the C, O, and CO atom fractions,

$$\begin{aligned} f^f = & f_{min}^f + \frac{E_v^f}{V_a} (1 - x_C) + \frac{k_B T}{V_a} [(1 - x_C) \ln(1 - x_C) - (1 - x_C)] \\ & + \frac{E_O^f}{V_a} x_O + \frac{k_B T}{V_a} [x_O \ln(x_O) - x_O] \\ & + \frac{E_{CO}^f}{V_a} x_{CO} + \frac{k_B T}{V_a} [x_{CO} \ln(x_{CO}) - x_{CO}]. \end{aligned} \quad (17)$$

The vacancy and defect formation energies were obtained from data from atomistic-scale simulations. Section 4 details the values and sources of each parameter used in our simulations. Since we use the GPM, the free energy density equations must be later converted to a grand-potential through the Legendre transformation in Eq. (9).

For the gaseous phase, we use a parabolic free energy density. The primary focus of this work is to model the evolution of carbon fibers during oxidation; the detailed prediction of the gas composition and evolution is not a primary goal at this time. In our simulations, the boundaries are open to gas diffusion, such that the produced gases can diffuse out of the system and new pure oxygen gas can diffuse in. Also, the diffusion of gaseous species at high temperatures is very fast, especially considering the length scale of the mesoscale model

(approximately 100 μm). Thus, the atomic fraction of each species in the gaseous phase is kept virtually at equilibrium throughout the simulation, enforced by a boundary condition. These conditions reduce the complexity of the composition profile in the gaseous phase and afford us the ability to use a simple parabolic free energy density to provide good computational efficiency. The parabolic coefficients and equilibrium concentrations are chosen appropriately to yield the phenomenological behavior of the gas during the oxidation process. The free energy density follows the form

$$f^g = \sum_{i=1}^4 \frac{A_i}{2} (x_i - x_i^{g,eq})^2, \quad (18)$$

where A_i is the parabolic coefficient and $x_i^{g,eq}$ is the equilibrium atomic fraction of species i ; the sum is over the C, O, and CO concentrations. In the gaseous phase, we assume that the gas is pure oxygen, and the equilibrium concentration is assumed to be $x_O^{g,eq} = 0.999$. The equilibrium concentration of C and CO is assumed to be zero. Setting the equilibrium concentration of CO to zero does not impede its production, since that is governed by the chemical reaction kinetics. We set these concentration to zero because no C or CO is expected to be present in the gas without the oxidation reaction. If one wants to model a gas with mixed species, these concentrations can be changed accordingly. In the gas phase, we assume that the vacancy concentration is

$$x_v = 1 - x_C - x_O - x_{CO}, \quad (19)$$

and it is close to zero since the lattice is filled with gas atoms.

The derivation of the grand-potential density from different free energy models has been presented for a binary mixture [40] and multicomponent mixtures [39]. Appendix A presents a summary of the grand-potential derivations from the free energy models that are used in our model.

2.2. Inclusion of chemical reactions in the phase-field model

The fibers evolve as O reacts with solid C to produce CO. In general, chemical reactions may occur between gaseous species within a volume or between a gaseous species and a solid species as a surface reaction. However, due to the diffuse nature of the free surface in our phase-field model, it treats gas and surface reactions identically. The rate at which the chemical reaction occurs is dictated by the reaction rate constant K and is represented by an Arrhenius function of temperature [47,48]

$$K = K_0 \exp\left(-\frac{Q}{k_B T}\right), \quad (20)$$

where K_0 is the pre-factor and Q is the activation energy. We introduce the rate of change of each chemical species depending on whether it is a reactant or a product, i.e.

$$\text{C(s)} + \text{O(g)} \rightarrow \text{CO(g)} \left\{ \begin{array}{l} \frac{\partial \rho_C}{\partial t} = -K \rho_C \rho_O, \\ \frac{\partial \rho_O}{\partial t} = -K \rho_C \rho_O, \\ \frac{\partial \rho_{CO}}{\partial t} = +K \rho_C \rho_O. \end{array} \right. \quad (21)$$

where K has units of $\text{m}^3/(\text{s atoms})$.

The contribution from the chemical reaction kinetics is added to the generalized diffusion equation from Eq. (1). Assuming a simple second order reaction between C and O atoms, the time evolution of species i becomes

$$\frac{\partial \rho_i}{\partial t} = \nabla \cdot M_i \nabla \frac{\delta F}{\delta \rho_i} \pm \tilde{K} \rho_O \rho_C, \quad (22)$$

where \tilde{K} is the effective reaction coefficient and the sign before \tilde{K} is negative when $i = \text{O}$ or C and positive when $i = \text{CO}$. $\tilde{K} = K$ when modeling the reaction of two gaseous species. In surface reactions, the reactant atoms adsorb to the surface of the fibers, react, and the product molecules desorb to the gas. In our mesoscale model, the diffuse surface

region is where the carbon in the fibers meets the oxygen in the gas and reacts. The number of reactions that occur across the surface depends on the varying atomic fractions of the reactants through the finite width of the surface region. The larger the width, the more reactions will occur. Therefore, $\tilde{K} = K/\delta_{int}$ for surface reactions, to make the reaction behavior independent of the interfacial width; this independence is confirmed in Section 3.1.

Applying the chain rule to expand the time derivative term [40] and rewriting the derivative of the free energy with respect to the number density as the chemical potential yields

$$\frac{\partial \rho_i}{\partial \mu_i} \frac{\partial \mu_i}{\partial t} + \frac{\partial \rho_i}{\partial \eta} \frac{\partial \eta}{\partial t} = \nabla \cdot M_i \nabla \mu_i \pm \tilde{K} \rho_O \rho_C. \quad (23)$$

Rearranging the terms in Eq. (23) and substituting in the susceptibility χ_i , we obtain the final evolution equation in our model,

$$\chi_i \frac{\partial \mu_i}{\partial t} = \nabla \cdot D_i \chi_i \nabla \mu_i \pm \tilde{K} \rho_O \rho_C - \frac{\partial \rho_i}{\partial \eta} \frac{\partial \eta}{\partial t}, \quad (24)$$

where we solve for the chemical potential variable of each species i (C, O, and CO). The atom fractions in each phase are calculated using the relationships from the free energy, and interpolated across the interfaces. We stop the reactions when the number density of the reactants falls below a small threshold to avoid negative values. Section 3.1 presents a verification of the surface reaction behavior.

2.3. Fully-coupled heat transport

As discussed previously, the temperature and oxidation behavior are tightly coupled. Therefore, we couple the phase-field oxidation model to heat transport. The heat transport in the system is modeled by a transient anisotropic heat conduction equation. The time evolution of the temperature T is described by:

$$c_p D \frac{\partial T}{\partial t} = \nabla \cdot \mathbf{k} \nabla T + \dot{q}, \quad (25)$$

where c_p is the specific heat in J/(g K), D is the density of the material in g/m³, \mathbf{k} is the anisotropic thermal conductivity tensor in W/(m K), and \dot{q} is the volumetric heat change in W/m³. The oxidation reaction is endothermic, with a positive enthalpy of reaction. We incorporate the enthalpy of reaction into the heat conduction equation as a local heat sink

$$\dot{q} = \Delta H_{reaction} \frac{\partial \rho_C}{\partial t}, \quad (26)$$

where ΔH has units of J/mol of products and $\partial \rho_C / \partial t$ is taken from Eq. (21). $\partial \rho_C / \partial t \neq 0$ at locations in the domain where chemical reactions are occurring, usually at carbon fiber surfaces.

As mentioned in the introduction, carbon fibers have much higher thermal conductivities in the axial direction than in the radial. The difference in the magnitude of the thermal conductivity value depends on the type of fiber and the manufacturing process. We assume that the value on the radial direction is two orders of magnitude smaller than the axial one [13]. This is included in the model using the thermal conductivity tensor \mathbf{k} . However, the tensor values must depend on the orientation of the fibers. Since the fiber structures in the phase-field model are represented by the variable field η_f , the fiber orientation can vary throughout the domain and therefore the value of \mathbf{k} must also vary.

To calculate the fiber orientation, we use the artificial heat flux approach established by Schneider et al. [49]. This approach consists of carrying out a preliminary calculation in which a pseudo-temperature gradient is imposed in each direction of the domain by setting a pair of cold and hot Dirichlet boundary conditions. An isotropic thermal conductivity value is assigned for the carbon fibers in this pseudo-temperature calculation, which must be much higher than the value in the bulk of the material. The authors suggest a zero thermal conductivity value for the bulk, though this can result in numerical difficulties. We have found that using a small value in the bulk is sufficient to

calculate the pseudo-temperature profile. Once the fibers are assigned a high thermal conductivity value and the bulk is assigned a low value, a steady-state heat conduction simulation (Eq. (25) with no heat source or time derivative term) is carried out in each of the x -, y -, and z -directions (just x - and y -directions for a 2D simulation). The heat preferably flows through the fibers due to their high thermal conductivity, indicating the fiber orientation. The local fiber direction vector \vec{d} is determined by

$$\vec{d} = \frac{\vec{q}_x + \vec{q}_y + \vec{q}_z}{\|\vec{q}_x + \vec{q}_y + \vec{q}_z\|}, \quad (27)$$

where \vec{q}_i is the local pseudo-heat flux resulting from the pseudo-temperature gradient in the i direction. The local fiber direction vector is used to calculate the local thermal conductivity tensor \mathbf{k} . The initial x -direction of the thermal conductivity tensor is arbitrarily chosen to be the direction of the fiber axis. This direction is then rotated to align with the fiber direction vector \vec{d} . The other two perpendicular directions fall on the radial plane of the fiber, and therefore have the same low value of thermal conductivity. The error associated with this approach is quantified in Section 3.2.

The local direction vectors are calculated once for the initial fiber structure and then used throughout the oxidation simulations to determine the local thermal conductivity tensors. This is possible because the fibers only shrink due to oxidation, such that no regions that were originally gas later become fiber.

2.4. Nondimensional parameters

The coupled heat conduction and phase-field equations must be solved simultaneously; however, their residual values may vary by many orders of magnitude, complicating the solve. Therefore, we transform the length l , time t , and energy e into the nondimensional length ξ , time τ , and energy ϵ by dividing by a constant factor of the same respective unit:

$$\xi = \frac{l}{l_0}, \quad (28)$$

$$\tau = \frac{t}{t_0}, \quad (29)$$

$$\epsilon = \frac{e}{e_0}. \quad (30)$$

We use the formation energy of a carbon vacancy in a fiber for the energy factor e_0 , the cube root of the atomic volume of carbon in the fiber for the length factor l_0 , and the diffusion coefficient of a carbon atom in the fiber to calculate the time factor t_0 . These values correspond to $t_0 = 4.3299 \times 10^{-4}$ s, $l_0 = 2.1524 \times 10^{-4}$ μm , and $e_0 = 3.9$ eV. Although the simulations are performed using the nondimensional parameters, the results are always converted back into actual units. Therefore, the units displayed in the results throughout the work are in actual units of length, time, and energy.

2.5. Model implementation

Our mesoscale model has been implemented in an open-source application based on the Multiphysics Object-Oriented Simulation Environment (MOOSE). Our mesoscale ablation modeling application is named Macaw and is available on GitHub [35]. The MOOSE framework is a non-linear, finite-element solver developed by the Idaho National Laboratory [37]. It is open-source with community development on GitHub. MOOSE uses the finite element library libMesh, a C++ library developed by the CFDLab at the University of Texas at Austin [50]; it also uses PETSc solvers [51,52] and is capable of large parallel simulations. A uniform mesh and adaptive time stepping were used in some of the simulations shown in this work. For the numerical solution, we applied Newton's method with a second-order backward differentiation scheme. The HYPRE BoomerAMG package from Lawrence Livermore National Laboratory [53] was employed to invert the Jacobian matrix

in the nonlinear solve. For all simulations shown in this paper, the automatic scaling capability in MOOSE was used to scale the residuals at each time step to improve computational performance. The mesh was generated using the mesh generator capabilities in MOOSE. First-order Lagrange elements were used, with 4-node quadrilaterals (QUAD4) in 2D meshes and a 8-node hexahedron (HEX8) for 3D meshes. A distributed mesh generated in MOOSE was used in 3D simulations to lower the memory usage, accompanied by a parallel output.

3. Verification

This section summarizes our efforts to ensure the accuracy of two aspects of the proposed model. We first evaluate the model performance for surface reactions and then quantify the error in the calculation of the anisotropic thermal conductivity tensor for randomly oriented fibers.

3.1. Comparison with surface reaction model

We check the accuracy of the surface reaction behavior modeled using the phase-field method. We consider a 1D domain with a pure carbon fiber phase on the left half of the domain and a pure gas phase on the right half. The C and O concentrations in the surface region between the fiber and gas phases follow a hyperbolic tangent with a characteristic width δ_{int} . Initially, the gas is pure atomic O and the reaction with C produces CO, $C(s) + O(g) \rightarrow CO(g)$. The fiber does not shrink because there is an infinite amount of C, which is imposed by having a zero reaction rate for the C variable; however, there is a zero flux boundary on the right such that there is a fixed amount of O that will decrease as CO is produced. We derived an analytical model that predicts the decrease of the oxygen in the system with time; the derivation is summarized in Appendix B. The final expression for the total amount of O in the system at a time t is

$$N_O(t) = \frac{1}{l_a} s_0 x_D^{e,0} \exp\left(-\frac{\delta_x}{4s_0} \bar{K} t\right). \quad (31)$$

The influence of the interface width on the oxygen consumption is clear in Eq. (31). When $\bar{K} = K/\delta_x$, this dependence on δ_x drops out. We modeled oxidation of our 1D fiber with Macaw using a domain size of 10 μm and an equivalent mesh refinement of 8 elements across the surface width. We start by analyzing a characteristic interface width of 1 μm , and then compare the results to a 0.5 μm one. The total number of elements across the domain was changed accordingly to maintain the same number of elements across the diffuse interface. The domain temperature was a constant 3000 K. The reaction rate constant followed an Arrhenius equation with pre-factor and activation energy shown in Table 1; the material properties are shown in the same table. The time step size changed due to adaptive time stepping; it started at 4.33×10^{-4} s and had a maximum value of 43.3 s. A zero-flux boundary condition was imposed on all variables.

Fig. 2 summarizes our comparison of the analytical surface reaction model to the phase-field implementation of surface reactions in Macaw. Fig. 2(a) shows the total amount of C, O, and CO in the system. The number of C atoms stays constant, the O atoms decrease according to the analytical Eq. (31), and the CO molecules increase. The error was quantified using the root-mean-square error (RMSE), i.e.

$$RMSE = \sqrt{\frac{\sum_i^n (N_{i,an} - N_{i,M})^2}{n}}, \quad (32)$$

where n is the number of measurements (time steps), $N_{i,an}$ is the number of O atoms from Eq. (31) and $N_{i,M}$ is the number of O atoms from the Macaw simulation. The predicted amount of O is very similar to that from the analytical model, with a RMSE (Eq. (32)) of 26.73 atoms, which is approximately 0.1% of the initial number of O atoms.

Fig. 2(b) depicts a log plot of the total amount of O atoms in the system computed using Macaw, compared to the analytical equation.

Table 1

Model parameters used in the fiber oxidation model. The description, value, and units for each parameter are shown. The references used to determine the values are also shown. The atomic volume of carbon in the fiber is listed for reference. For the LHS sampling used in the SA from Section 4, each parameter was assumed to follow a normal distribution with a standard deviation equal to 10% of the mean.

Description	Parameter	Value	Units	References
Reaction rate	K_0	9.46×10^3	$\text{cm}^3/(\text{mol s})$	[47,48]
	Q	0.5	eV/atom	[47,48]
Thermal conductivity	$k_{f,ax}$	50	W/(m K)	[18]
	$k_{f,rad}$	0.5	W/(m K)	[22]
	k_g	0.18	W/(m K)	[54]
Diffusion coefficient	D_C^f	1.07×10^{-12}	cm^2/s	[55]
	$D_{O,CO}$	3.00×10^{-3}	cm^2/s	[45,46]
	$D_{C,O,CO}^g$	1.00	cm^2/s	[56,57]
Specific heat	c_p^f	2.50	J/(g K)	[18]
	c_p^g	1.25	J/(g K)	[58]
Density	ρ_f	2.00	g/cm^3	[18]
	ρ_g	1.30×10^{-4}	g/cm^3	–
Surface energy	σ_{int}	0.20	J/m^2	[59–61]
Reaction energy	ΔH	100	kJ/mol	[62]
Formation energy	E_C^f	3.90	eV/atom	[63–65]
	E_O^f	6.10	eV/atom	[66]
	E_{CO}^f	6.31	eV/atom	[67]
Energy coefficient	A_C^g	7.82×10^1	eV/nm^3	–
	$A_{O,CO}^g$	3.91×10^{-4}	eV/nm^3	–
Atomic volume	V_a	9.97×10^{-3}	nm^3/atom	–

The reaction rate constant can be obtained from the slope of this curve. The Macaw data was fitted to a line, and the effective slope had an error of 0.5% compared to the analytical one for a mesh refinement equivalent to 8 elements across the interface width. The error decreases with increasing mesh refinement and this decrease is consistent with the theoretical behavior of first-order finite elements.

Fig. 2(c) and (d) show the amount of oxygen and the logarithmic plot for two different interface widths, to ensure that the results are independent of the width. We use $\delta_{int} = 0.5$ and 1.0 μm . The two simulation results overlap, confirming that the oxidation rate predicted by our phase-field oxidation model is independent of the interface width.

3.2. Quantification of fiber direction error

In this section, we quantify the error in the average fiber direction calculated using the artificial heat flux approach by Schneider et al. [49]. The domain used for this analysis was a 2D $120 \times 120 \mu\text{m}$ square with 480×480 first-order elements. The fibers were initialized from a binary image, and we calculated the angle of the features in the image. We modeled a case with a 110 μm long fiber fully contained within the domain and one with a long fiber that crossed the domain boundaries. We created binary images with fibers oriented with angles of 0° , 30° , 45° , 60° , and 90° , and used those to test the accuracy of the artificial heat flux calculation. In the 2D domain, the fibers were represented by rectangles with a thickness of 7 μm . The fibers had an isotropic thermal conductivity of 6.7×10^{-4} W/(m K) and the bulk had an isotropic thermal conductivity one hundred times smaller. The cold Dirichlet boundary condition was 1000 K and the hot one was 2000 K for both the temperature variables.

The error in the angle calculation using the artificial heat flux approach is shown in Fig. 3(a). The average error for all cases was smaller than 3° , though the error was larger with embedded fibers than with long fibers. This is because the error was mostly concentrated at the ends of the fiber, where the heat is entering or leaving. This observation is consistent with the findings of Semeraro et al. [68], who performed a 3D analysis of the error associated with the artificial heat flux approach from Schneider et al. [49].

The anisotropic thermal conductivity of the fiber calculated using the artificial heat flux method has a significant impact on the heat

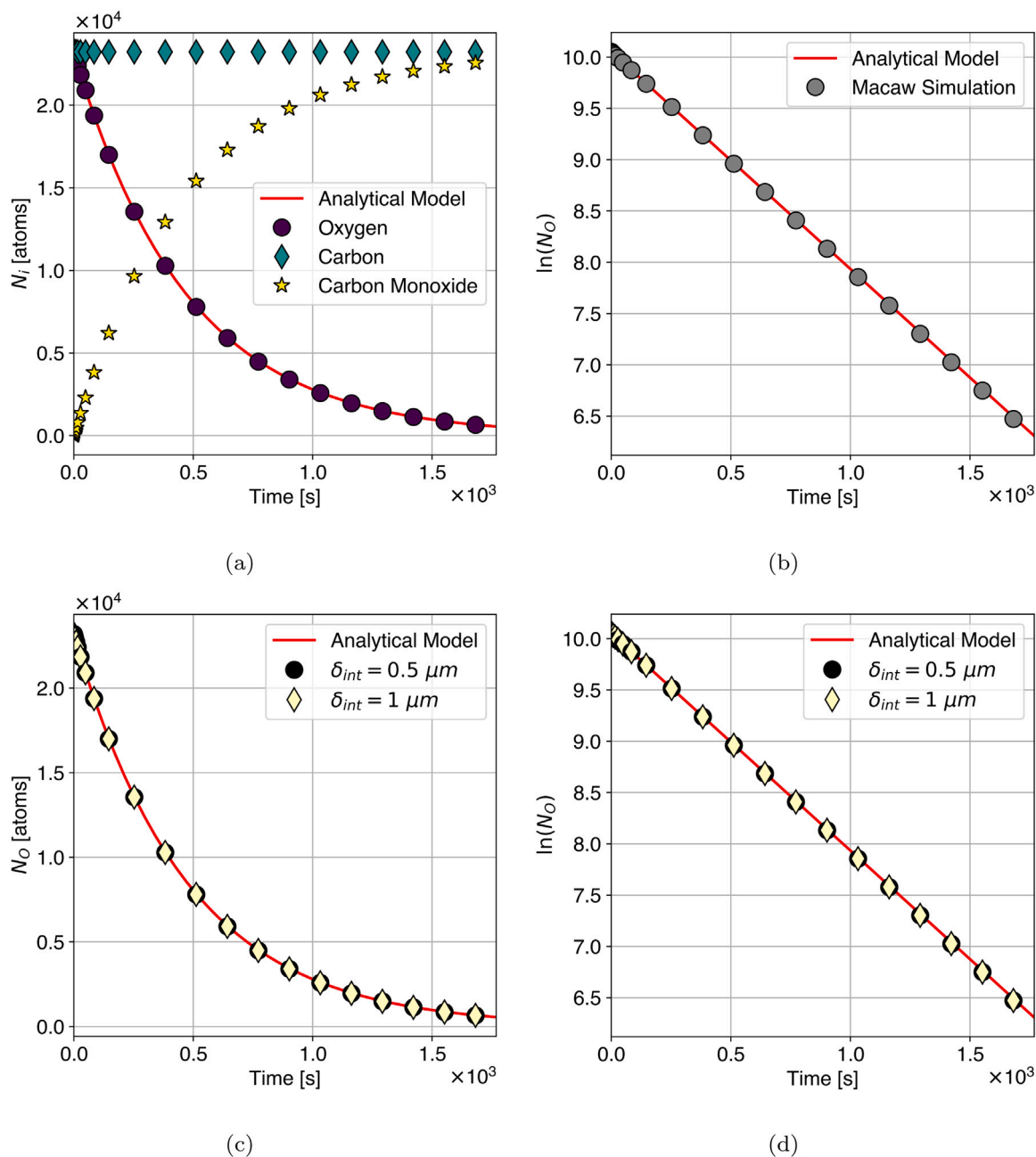


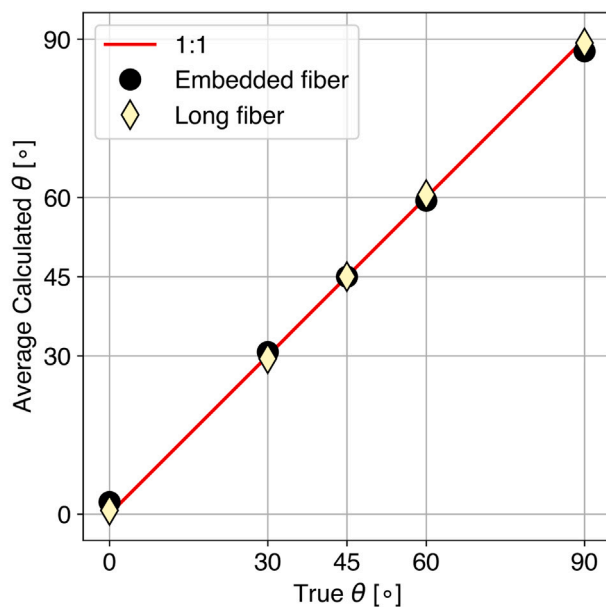
Fig. 2. Results of the 1D surface reaction verification. (a) Time evolution of the total amount of C, O, and CO versus time from the phase-field model with $\delta_{int} = 1.0 \mu m$ and the amount of O from the analytical model. (b) Logarithmic plot of the total amount of O versus time from the phase-field ($\delta_{int} = 1.0 \mu m$) and analytical models. (c) and (d) Comparison of the results for two different interface widths, $\delta_{int} = 0.5$ and $1.0 \mu m$. The results were independent of the interface width.

transport. We calculated the temperature throughout the domain with an embedded fiber oriented at 30° using an isotropic high thermal conductivity in the fiber and using the anisotropic thermal conductivity, as shown in Fig. 3(b) and (c), respectively. In the isotropic case, the temperature throughout the fiber is nearly constant. In the anisotropic case, heat is only transported easily in the axial direction, resulting in angled isotherms perpendicular to the axial direction and changing the temperature profile in the gas around the fiber.

4. Sensitivity analysis

Having verified that our mesoscale fiber oxidation model is functioning correctly, we performed a sensitivity analysis (SA) to understand the impact of the material properties on the oxidation behavior. This comprehensive analysis simultaneously studied the effect of all

the phase-field model parameters. The software DAKOTA [69], which is developed by the Sandia National Laboratories, was used to carry out the SA. Latin Hypercube Sampling (LHS) was used to generate near-random values for the 20 model parameters, following a normal distribution. A total of 1000 phase-field simulations were carried out using sampled values for all 20 parameters. For the thermophysical properties, the mean values were taken from the literature. Table 1 shows the description of each parameter, its mean value, and the reference literature. Since the actual values for PICA carbon fibers varies widely with the manufacturing process, similar graphitic structures were used to narrow the parametric space for the properties. A similar approach was taken to define the properties of the gaseous phase, where the thermophysical properties were based on reported values for oxygen gas. We assumed that the species had the same diffusion coefficient in the gas, and that C and CO had the same diffusion



(a)

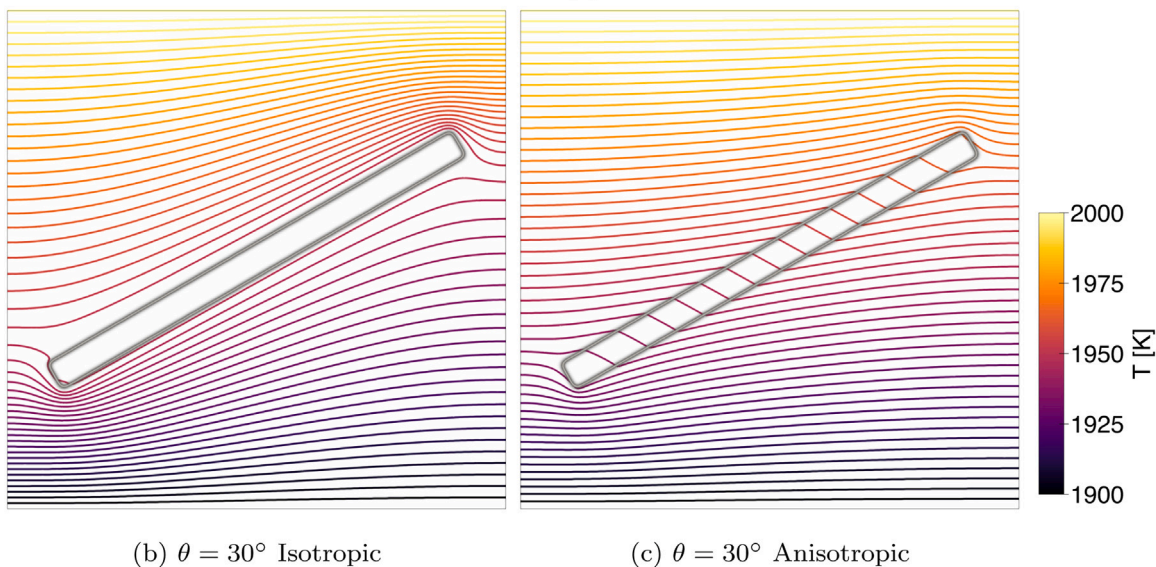


Fig. 3. Investigation of the approach for the anisotropic thermal conductivity. (a) Calculated fiber angle vs. true angle for the embedded and long fiber cases. (b) Temperature profile with a high isotropic fiber thermal conductivity. (c) Temperature profile with an anisotropic fiber thermal conductivity. The domain size is $120 \mu\text{m} \times 120 \mu\text{m}$, and the fibers are $7 \mu\text{m}$ wide.

coefficients in the fiber. The density of the gas was estimated based on an ideal gas at 3000 K and 1 atm. We also assume that the parabolic energy coefficients of O and CO are equal. The standard deviation of the normal distribution used for each parameter was assumed to be equal to 10% of the mean values. The reaction rate constant varies with temperature as shown in Eq. (20), so the pre-factor and activation energy were independently analyzed in the sensitivity study. At this stage of our model, the other thermophysical properties were assumed to be constant with temperature.

The simulation was performed in a cylindrical coordinate system (referred to as RZ), where the fiber is parallel to the y -axis. A relatively small fiber was used to reduce the computational costs associated with running 1000 phase-field simulations to obtain the SA data. The fiber had an initial radius of $5 \mu\text{m}$ and a length of $50 \mu\text{m}$, and we used a diffuse interface width of $0.5 \mu\text{m}$ resolved with 4 elements. The 2D RZ domain was $55 \mu\text{m} \times 10 \mu\text{m}$. The top boundary was open to gas

flow in or out, with a Dirichlet boundary condition on the chemical potential of O and CO equal to zero, maintaining the gas at equilibrium. The top also had a Dirichlet boundary condition on the temperature, with a value of $T = 3000 \text{ K}$, to represent the incoming heat that the fiber would experience under atmospheric-entry conditions. A zero-flux boundary condition was set for all other variables and boundaries. The time step size started at 4.3 s and grew until it reached a value that had a good numerical performance according to the optimal condition of converging in 4 non-linear iterations. The system was initialized with the equilibrium atomic fractions in the fiber and gas.

Fig. 4 shows an example of the microstructure evolution of the fiber in the RZ coordinate system. The contours represent the outer edge of the carbon fiber. The rectangular outermost contour is the initial state of the fiber, and the inner ones are subsequent stages during the oxidation simulation. The oxidation occurs at the surface, and the sharp corner from the initial cylindrical shape transforms into a more oblong

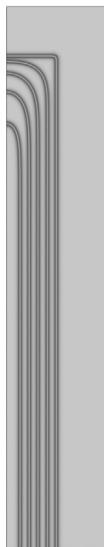


Fig. 4. An example of the fiber oxidation predicted by the axisymmetric simulations for the SA. The outermost rectangular shape is the initial condition, with subsequent inner profiles representing later times. The carbon fiber is immersed in pure O gas and the temperature at the top boundary is fixed at 3000 K. The top boundary is open for entrance of O and exit of CO. The domain is $55 \mu\text{m} \times 10 \mu\text{m}$, and the initial fiber is $50 \mu\text{m}$ long with a radius of $5 \mu\text{m}$.

shape whilst the whole fiber becomes thinner. The response of interest was the time it took for the fiber to disappear, determined by when the volume fell below a small threshold. We refer to this quantity as the oxidation time.

Fig. 5(a) presents the sensitivity of the oxidation time to each input parameter, where the input parameters are described in Table 1. The sensitivities were obtained by first fitting a linear regression to the scatter data from the simulation results. The sensitivity is the slope of the linear fit for the response vs. input parameter. The values were first normalized to the means of each parameter. Then, the highest sensitivity was taken to be equal to one and the other sensitivities were normalized to that absolute value. The sign of the sensitivity indicates that an increase in the parameter value causes an increase (positive) or decrease (negative) in the oxidation time.

The reaction-rate pre-factor K_0 and activation energy Q were by far the most influential input parameters. They were both many times more sensitive than all the other parameters, indicating a reaction-limited behavior. The activation energy was twice as sensitive as the pre-factor, since the reaction rate depends exponentially on Q but only linearly on K_0 .

The thermal conductivities and reaction energy, which impact the steady-state temperature profile, were the next most sensitive parameters, though they were much less sensitive than the reaction rate parameters and only slightly more sensitive than other parameters. The thermal conductivity of the fiber, both in the axial and radial directions, were more sensitive than the gas conductivity and the reaction energy.

The oxidation time was not very sensitive to the specific heats and densities of the gas and fiber, which impact the transient temperature behavior. The densities were more sensitive than the specific heats. The low sensitivities of these parameters indicate that steady state heat conduction is a reasonable assumption and we use it later in 2D and 3D multiple fiber simulations to reduce the computational cost.

The low sensitivities of the surface energy, diffusion coefficients, and free energy parameters indicate that the fiber loss during the simulations is due to the chemical reaction, not energy-driven evolution. This further indicates our success in developing a model that ensures reaction-controlled behavior.

Having established that the fiber oxidation is dominated by the reaction rates, we carried out an additional SA to evaluate the importance of the temperature boundary condition on the top surface. Out of the full set of parameters varied in the first SA, in this additional SA we only varied the values of the chemical reaction kinetics, thermal conductivities, and reaction energy. The value of the temperature on the top boundary was varied with a mean value of 2500 K. Thus, a total of 7 parameters were analyzed, with 770 near-random values sampled from normal distributions using the LHS technique. All other parameters were held at their mean values shown in Table 1. The sensitivities were normalized using the same procedure previously described. Fig. 5(b) summarizes the sensitivities for this second analysis.

The domain temperature was the most influential parameter, followed closely by Q . The sensitivity of K_0 was less than half that of Q . The high sensitivity of the ablation to the top temperature is expected since the reaction rate is an exponential function of temperature, as shown in Eq. (20), like Q .

The thermal conductivities and reaction energy were again much less sensitive than the parameters related to the reaction rate. Interestingly, their sensitivities did not follow the same trends as seen in the first SA. The axial thermal conductivity of the fiber was the most sensitive, then the reaction energy, and the radial and gas thermal conductivities were the least sensitive. There are two likely causes for these changes. First, these sensitivities were the slopes of linear fits to 770 data points that did not have clear trends. So, these slopes may not have been statistically significant. Second, the impact of the thermal conductivities may have been dependent on the temperature, which was varied in this SA.

The results from both SAs indicate that for this single fiber in the presence of oxygen gas, the reaction rate, determined as a function of K_0 , Q , and T , is the most influential parameter. We do expect other parameters to be more influential in larger domains, where the porous carbon fiber substrate hinders the diffusion of reacting species. The competition between the reactivity of the surface of the fibers and the diffusion of reactants within the material, which can cause in-depth oxidation, is likely to be pronounced as reported by previous works [29,31]. We will explore the oxidation behavior for more fibers and in both 2D and 3D in the next section.

5. Carbon fiber oxidation by oxygen gas

In this section, we apply our temperature-dependent phase-field oxidation model to simulate the surface oxidation of multiple fibers. Ideally, we would compare the simulation results to experimental data. However, the data available in the literature uses samples that would be prohibitively large with our model. For example, Panerai et al. [70] measured the carbon loss in a 22 mm diameter cylindrical slug of FiberForm that was 22 mm long. Modeling such a large 3D domain with our phase field model would require on the order of 1×10^{14} elements. Thus, in this work we do not compare with experimental data, but rather demonstrate the capabilities of the model. If data from microscale experiments are obtained in the future, our model could be validated.

We demonstrate the capabilities of our phase field model by first simulating the oxidation of multiple carbon fibers in 2D both under a temperature gradient and with an incoming heat flux. Next, we simulate the oxidation of 3D cylindrical carbon fibers under a temperature gradient.

To estimate the temperatures to use in the simulations, we turn to reported temperatures for previous missions and experiments. Stardust's probe experienced heat fluxes as high as 1100 W/cm^2 [2]. Early experiments at 570 W/cm^2 recorded an in-depth temperature above 3000 K at approximately 1.22 cm within the sample [5]. For the Mars Science Laboratory capsule that took the rover Curiosity to Mars, the heat shield had advanced instrumentation that recorded temperatures on the order of 1500 K [71]. From these findings, it seems appropriate

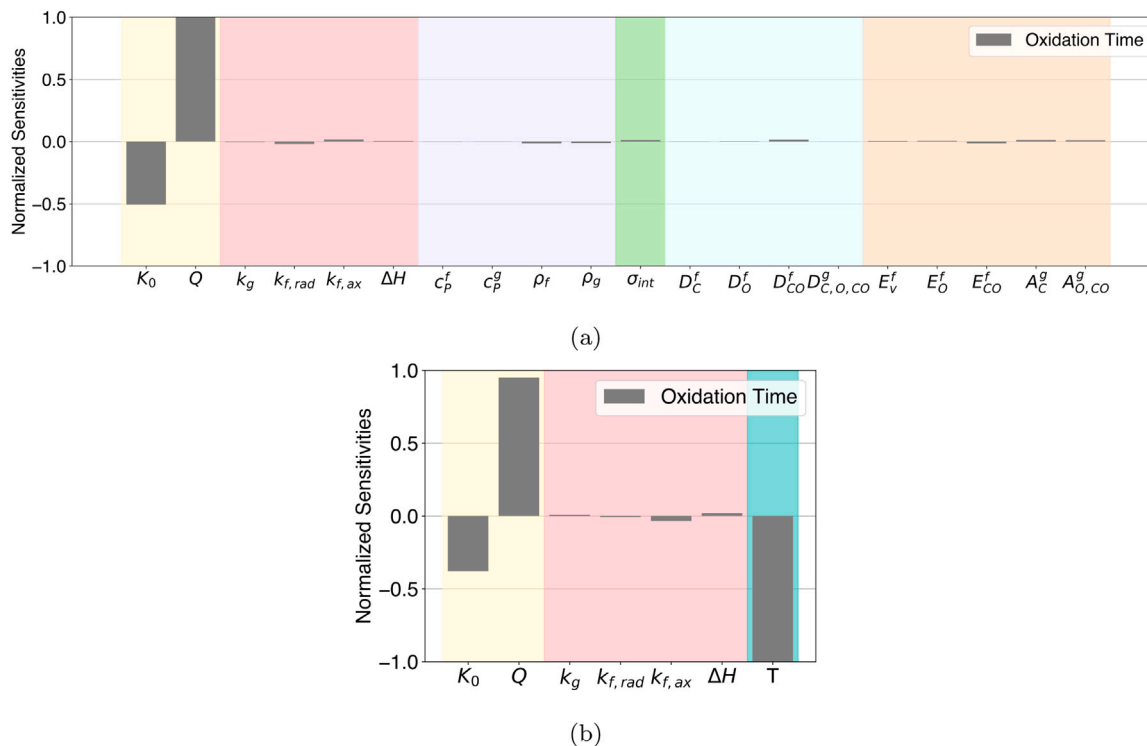


Fig. 5. Sensitivity of the oxidation time with respect to each model parameter. (a) shows the results of the SA with all thermophysical properties and model parameters at a constant temperature of 3000 K. The reaction rate constant parameters are colored yellow, the thermal conductivities and reaction energy are colored red, the specific heat and densities are purple, the surface energy is green, the diffusion coefficients are blue, and the free energy parameters are orange. The most impactful parameters were those associated with the reaction rate constant. (b) shows the results from the second SA, where the domain temperature was included with the physical parameters for heat transport. The temperature was the most impactful parameter, followed by the activation energy.

to chose a top temperature of 3000 K. To estimate the gradient across the mesoscale domain, we analyzed reported in-depth temperatures from the work of Weng and Martin [27]. For a 1D analysis at a fixed surface temperature of 1644 K for 60 s, the temperature difference up to 1 cm in the domain was around 800 K. If we assume a linear profile, this yields a change in temperature of about 1 K per 10 μm as a reasonable temperature gradient in our carbon fiber oxidation simulations. The temperature gradient is imposed using Dirichlet boundary conditions on the top and bottom boundaries. For the 2D heat flux case, we initialized the system with an uniform temperature equal to 3000 K and applied two heat flux magnitudes as a Neumann boundary condition on the top boundary, with values of $\dot{q} = 0.01 \text{ W/cm}^2$ and $\dot{q} = 0.1 \text{ W/cm}^2$. These values are much lower than the expected heat flux during an atmospheric entry, which can be up to 1100 W/cm^2 [2]. In our mesoscale domain (around 100 μm), we do not account for all the heat dissipation mechanisms that the PICA TPS has in place during entry conditions. Therefore, we have to reduce the heat flux to accommodate for the lack of heat dissipation. In these simulations, the oxidation happens on the surface of the carbon fibers and consume a much smaller amount of heat than the complete ablation of the PICA.

According to the results of the SA discussed in Section 4, the oxidation of the carbon fibers was highly sensitive to K_0 and Q , but not to the other material properties. Therefore, to simplify the calculation, we assume that they are constant with temperature and are equal to the values shown in Table 1 for all simulations in this section.

5.1. 2D simulations

In this section, we demonstrate the carbon fiber oxidation coupled with heat conduction in 2D with multiple carbon fibers. We begin with simulations of the fiber oxidation with fixed temperatures on the top and bottom boundaries for two cases, one with 12 straight fibers with varying diameters and one with 6 curved fibers with all the same

diameter. We then consider two cases with 8 straight fibers and applied heat fluxes. In all cases, an initial artificial heat flux calculation [49] was used to determine the local orientation of all the fibers to calculate the anisotropic thermal conductivity.

We used a $120 \times 120 \mu\text{m}$ domain. The interface width was 1.0 μm resolved with four elements. The top boundary had a Dirichlet boundary condition for the O and CO chemical potentials that enforced the equilibrium concentration. A zero-flux boundary condition was set for all other phase field variables and boundaries.

In the fixed boundary temperature cases, a Dirichlet boundary condition was applied on the top and bottom boundaries, where the top temperature was fixed at 3000 K and the bottom at 2988. As discussed in Section 4, the SA results indicated that transient heat transport had little impact on the results with fixed temperature boundary conditions, so we assumed steady-state heat transport to reduce computational cost. The timestep started at $4.3 \times 10^{-3} \text{ s}$ and reached a maximum value of 4.3 s. The system was initialized with the equilibrium atomic fractions in the fiber and gas.

Fig. 6(a) and (d) show the initial fiber structures in gray; the gaseous region is colored by the initial temperature profile, which decreases from 3000 K at the top boundary to 2988 K at the bottom. The effect of the anisotropic thermal conductivity is evident in the surrounding temperature profile. This is especially evident with the curved fibers in Fig. 6(d).

Fig. 6(b) and (c) show the oxidation of the straight fibers with various diameters. The gaseous region is shaded by the atomic fraction of CO. Initially, the fraction of CO was zero and there was O everywhere in the system. CO was produced due to the oxidation of the fibers and then escaped through the top boundary, when possible. Thicker fibers took a longer time to disappear, since they had more mass to be consumed. Because diffusion of CO through the fiber is very slow, CO accumulated below the long thick fiber that spanned the full width of the domain. When this fiber got thinner, diffusion was facilitated and

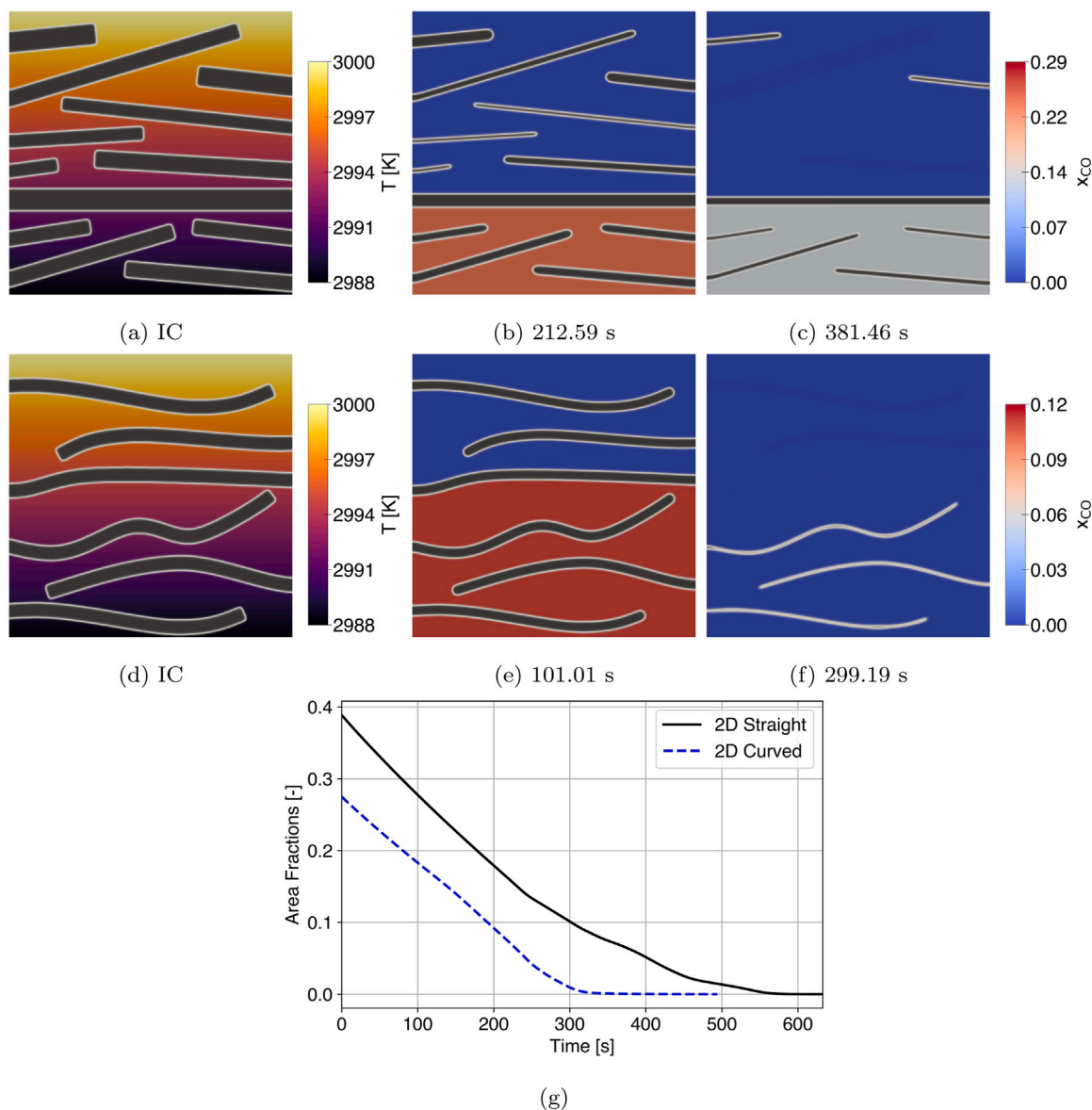


Fig. 6. Results from the 2D multiple fiber oxidation simulations in a $120 \times 120 \mu\text{m}$ domain. (a)–(c) show the evolution of the straight fiber structure over time, starting at the initial condition (IC). (d)–(f) show the evolution of the curved fibers. In (a)–(f), the fibers are shown in gray; in the IC, the gas phase is colored by the temperature; in the subsequent images, the gas phase is colored by the fraction of CO.

eventually the CO was able to escape the system from the top boundary. The maximum fraction of CO achieved during the simulation time is shown as the maximum value in the colorbar. Fig. 6(e) and (f) show the oxidation of the curved fibers. Again, CO accumulated below the fiber that spanned the full domain width. Once it disappeared, all of the CO could escape. The maximum CO achieved was lower than with the straight fibers, likely because there were fewer fibers so less oxidation took place.

Fig. 6(g) shows the time evolution of the area fraction of the carbon fibers during the simulations. The straight fiber case had a higher initial area fraction of fiber than the curved fiber case, and therefore it took longer to oxidize. In both cases, the slope of the constant area fraction with time was fairly constant through most of the oxidation but slowed when the fibers were very thin. The slopes were similar, even though the straight-fiber case had more fibers and thus more C to react.

The oxidation happened similarly in both cases. Initially, O was present throughout the domain and there was no CO. The O reacted with C at the surface of the fibers, eating away at the fibers and producing CO. The CO diffused through the domain and escaped out

the top boundary. More O diffused down from the top boundary, replenishing the concentration and allowing the oxidation reaction to continue. Due to the high gas diffusion coefficients the concentration gradients in open regions were very small. Both cases included a long fiber that crossed the domain, cutting off the lower region that could get depleted of reactants. Thus, fibers below the long fiber reacted with the available oxygen, but the oxidation was then limited by the diffusion of oxygen through the long fiber. For this reason, the fibers below the long fiber oxidized slower than those above. When the long fiber was consumed, O again reached the lower fibers and their oxidation accelerated. This phenomenon was exaggerated due to our 2D domain, but a less pronounced behavior could occur in 3D if a structure had reduced gas flow.

In the previous simulations with fixed temperatures on the top and bottom boundaries, the domain temperature was fairly constant. For this next case, we applied a heat flux at the top boundary and thermally insulated the other boundaries. The incoming heat flux from the top boundary caused an increase from the initial temperature of 3000 K. However, the endothermic oxidation reaction absorbs heat.

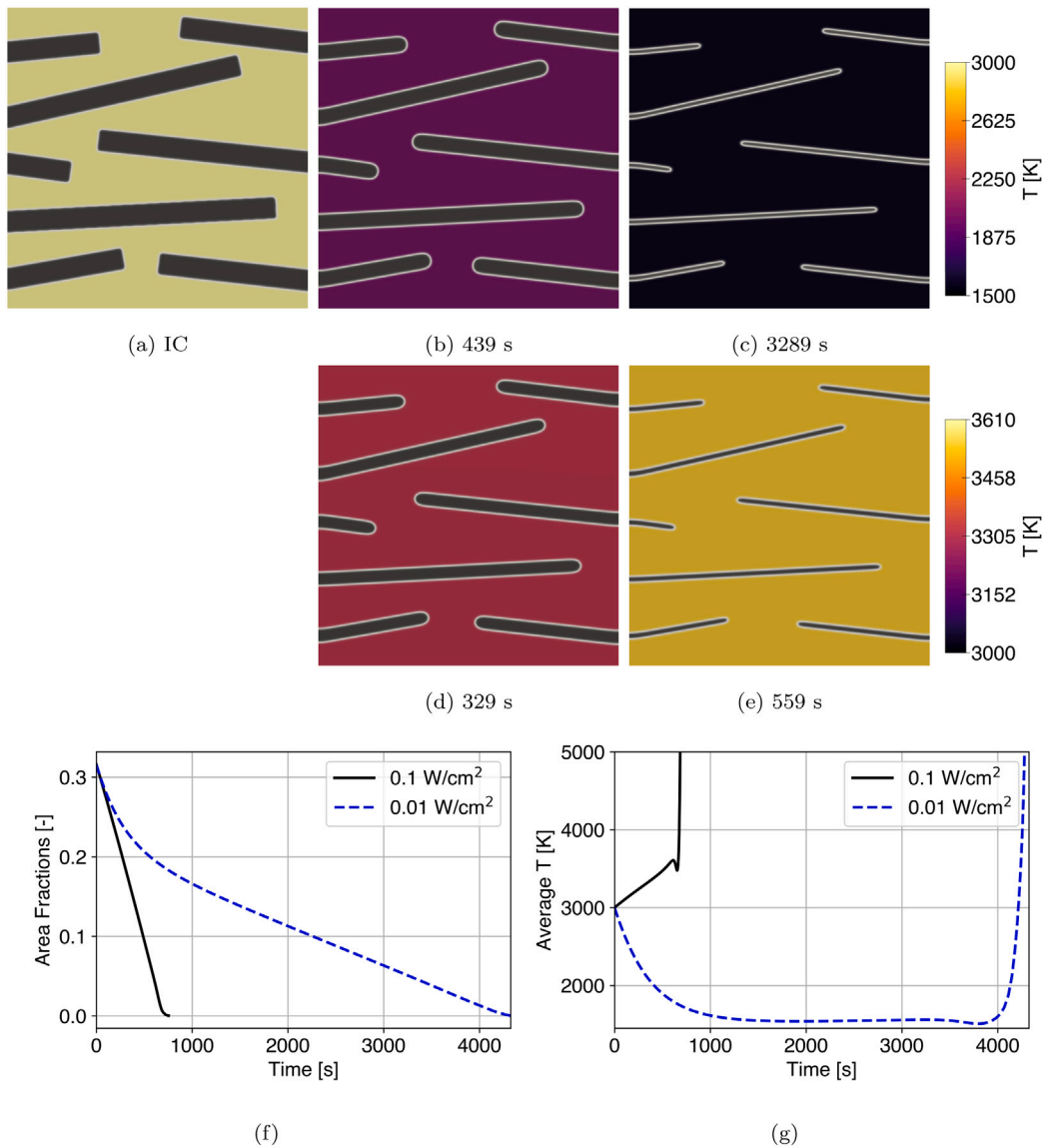


Fig. 7. Results from the carbon fiber oxidation simulations for different heat flux conditions in a $120 \times 120 \mu\text{m}$ domain. (a)–(c) show the evolution of the fibers under a heat flux of $\dot{q} = 0.01 \text{ W/cm}^2$, starting at the IC. (d) and (e) show the evolution of the fibers under a heat flux of $\dot{q} = 0.1 \text{ W/cm}^2$. (f) shows the evolution of the fiber area fraction with time. (g) shows the evolution of the average domain temperature over time.

We analyzed the competition between the incoming heat flux and the heat absorbed by the oxidation by comparing the behavior from the two heat flux values discussed above ($\dot{q} = 0.01 \text{ W/cm}^2$ and $\dot{q} = 0.1 \text{ W/cm}^2$). The microstructure is composed of 8 carbon fibers of a diameter of approximately $7 \mu\text{m}$ in a $120 \times 120 \mu\text{m}$ domain. The boundary conditions for the phase field variables were identical to those used in the previous simulations. To fully capture the competition of the incoming heat flux with the endothermic reaction heat sink, we modeled the transient heat conduction.

Fig. 7(a)–(c) present the time evolution of the lower heat flux case, where $\dot{q} = 0.01 \text{ W/cm}^2$, starting from the initial condition. The gas phase is colored by the temperature, which decreases with time until the fibers are very thin. Fig. 7(d)–(e) show the evolution of the microstructure under the higher heat flux, $\dot{q} = 0.1 \text{ W/cm}^2$, where the temperature increases with time. Fig. 7(f) and (g) show the evolution of the area fraction and average domain temperature with time. The higher heat flux caused a sharper and more linear decrease in the area fraction due to a slow increase in the average domain temperature. Since the reaction rate is a function of temperature, it increased with the increasing temperature, accelerating the oxidation. The lower heat

flux had a slower decrease in the area fraction, since the temperature decreased and slowed the oxidation. The domain temperature and oxidation rate stayed constant after around 1000 s and the area then decreased linearly until the fibers began to disappear.

For the higher heat flux ($\dot{q} = 0.1 \text{ W/cm}^2$), the average domain temperature increased linearly until the fibers began to disappear. For the lower flux ($\dot{q} = 0.01 \text{ W/cm}^2$), the temperature decreased and then held constant until the fibers begin to disappear. In both cases, there was a decrease in the temperature when the fibers began to disappear, caused by the increased access of O to C in the very thin fibers. This resulted in an increase in oxidation and more heat absorption. Once the carbon fibers disappeared, the domain temperature increased sharply due to the lack of heat dissipation from oxidation, the constant incoming heat flux from the top boundary, and the zero heat flux at the other boundaries. This final increase in the average domain temperature demonstrated that the endothermic reaction enthalpy is a key aspect of heat protection in the PICA TPS. Also, because our oxidation model is fully coupled with heat conduction, it can capture the close connection between the oxidation and the temperature.

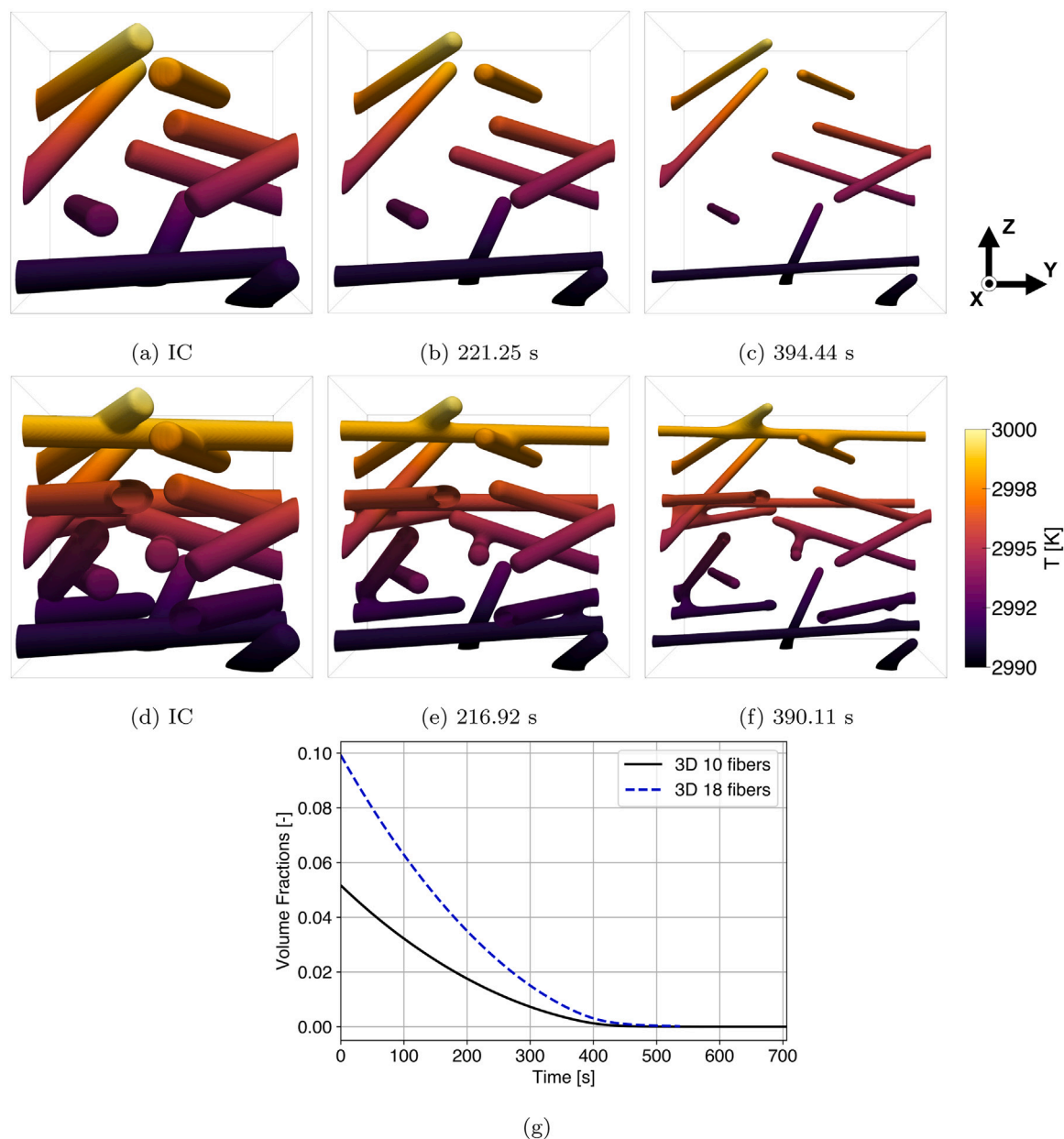


Fig. 8. Results from the 3D multiple fiber oxidation simulations in a $100 \times 100 \times 100 \mu\text{m}$ domain. (a)–(c) show the evolution of 10 cylindrical carbon fibers over time, starting at the IC. (d)–(f) show the evolution of 18 fibers initially in contact. (g) shows the evolution of the fiber volume fraction with time for the two cases. In (a)–(g) the fibers are shown with contours drawn at values of $\eta_f = 0.1$ and 0.9 and colored by the temperature.

5.2. 3D simulations

In this section, we show simulations of the fiber oxidation and heat transport for two 3D cases. The 3D simulations present a more realistic fiber configuration and transport conditions since the gas and heat can transport around the fibers; however, they are also much more computationally expensive. We considered straight cylindrical fibers dispersed in a $100 \times 100 \times 100 \mu\text{m}$ domain. The fibers had an initial radius of $5 \mu\text{m}$, and their length and orientation varied. The diffuse interface width was $2.0 \mu\text{m}$ resolved with 4 elements. The first case had 10 fibers dispersed throughout the domain such that they are not in contact; the second had 18 fibers that are in contact. The boundary conditions were similar to those in the 2D simulations, with fixed O and CO concentrations on the top boundary. The top boundary had a Dirichlet boundary condition of $T = 3000 \text{ K}$ and the bottom surface $T = 2990 \text{ K}$. The timestep size varied the same as in the 2D simulations and

the system was again initialized with the equilibrium atomic fractions in the fiber and gas.

Fig. 8(a)–(f) present the time evolution of the 3D carbon fibers during the oxidation process. The fibers are shown with 3D contours drawn at values of $\eta_f = 0.1$ and 0.9 that are colored by the local temperature. The oxidation occurred on the surface of the fibers, so they grew thinner and shorter with time until they disappeared. The evolution of the 10 fibers is shown in Fig. 8(a)–(c) and of the 18 fibers is shown in Fig. 8(d)–(f). Fig. 8(g) shows the time evolution of the volume fraction of the carbon fibers. Note that when fibers intersect a domain boundary at an angle, the order parameters evolve such that the fibers meet the boundary at a right angle due to the no-flux boundary conditions. This results in some thickening of the fibers at the boundaries.

As shown in Fig. 8(a)–(f), the oxidation behavior in the 3D simulations was similar to what was seen in the 2D simulations. O was consumed as it reacted with C at the surface of the fibers, producing

CO. The fibers shrank due to this reaction. CO transported to the top boundary and left the domain; new O entered at the top boundary. The flow of the gas was easier in the 3D domain, such that no O depletion occurred. The primary difference between the 10 and 18 fiber cases was that in the 18 fiber case the contact area between fibers was slower to oxidize. After the bulk of the fibers was consumed, dispersed fragments of the carbonaceous structure were left from the contact regions. These small pieces would normally spallate and be removed by the gas flow around the capsule during an atmospheric entry. However, since spallation is not included in the model, these regions remained and continued to oxidize.

The initial reduction in volume fraction was faster in the 18 fiber case than in the 10 fiber case, as shown in Fig. 8(g). This is because more C was exposed to O with 18 fibers than with 10, allowing faster consumption of the fibers. Since the flow of O was unimpeded, these reactions continued unabated such that the two cases reached a zero fiber volume fraction at about the same time. This is different than what occurred in the 2D cases, in which the change in the fiber area fraction was fairly independent of the number of fibers and the curved case with fewer fibers reached a zero area fraction much sooner than the straight-fiber case. This is likely because the reactions lower in the domain were deprived of oxygen in the 2D simulations but not in the 3D, and because the fibers were only exposed to O on their top and bottom faces in 2D but they were exposed from all directions in 3D.

6. Conclusions

In this paper, we presented a novel mesoscale phase-field oxidation model that is coupled with heat conduction. The multiphysics model captures the loss of fiber volume that is driven by temperature-dependent chemical reaction kinetics. The phase-field model equations are solved simultaneously with the heat conduction equations using the MOOSE Framework in the new Macaw application.

The model was verified against a novel analytical solutions for surface reactions. The model results are independent of the interface width and have a great agreement with the analytical model. For a mesh refinement equivalent to 8 elements over the interface width, the error in the oxidation rate is less than 0.5%.

A SA of the model parameters and thermophysical properties revealed that the reaction rate pre-factor, activation energy, and the surface temperature were by far the most sensitive parameters. This indicated that the model was indeed dominated by the reaction kinetics, as intended. The low sensitivity of the specific heats and densities indicated that the heat transport could be assumed to be at steady state.

The model capabilities were demonstrated for 2D and 3D simulations of the oxidation of multiple carbon fibers dispersed in oxygen gas. The oxidation of carbon fibers exposed to gas is relevant to the outermost region of the PICA TPS. Thicker fibers were shown to be consumed slower than thinner fibers. It was also shown that the fibers far from the top surface were starved of oxygen in 2D but not in 3D, since in 3D the oxygen could flow around the fibers. Thus, the model is able to account for the impact of gas flow on the oxidation behavior. Moreover, it was demonstrated that the coupled oxidation with heat conduction captures changes in the domain temperature over time that are caused by the competition of the incoming heat flux and the endothermic reaction enthalpy. The change in the domain temperature impacts the reaction rate, which causes a feedback effect on the temperature.

CRedit authorship contribution statement

Marina Sessim: Conceptualization, Methodology, Investigation, Software, Writing – original draft, Visualization, Validation. **Linyuan Shi:** Writing – review & editing. **Simon R. Phillpot:** Conceptualization, Resources, Writing – review & editing, Funding acquisition, Project administration, Supervision. **Michael R. Tonks:** Conceptualization, Methodology, Resources, Writing – review & editing, Funding acquisition, Project administration, Data curation, Supervision.

Declaration of competing interest

The authors declare that they have no known competing financial interests or personal relationships that could have appeared to influence the work reported in this paper.

Data availability

The data that support the findings of this study are available from the corresponding author upon reasonable request. The Macaw source code and input files are openly available on GitHub at <https://github.com/tonkmr/macaw>.

Acknowledgments

This work was supported by the Early Stage Innovations (ESI) NASA, United States Grant 80NSSC18K0250. The authors would like to thank our collaborators at NASA Ames Research Center, Joshua Monk and Nagi N. Mansour, for valuable discussions.

Appendix A. Grand-potential formulation for the dilute solution and parabolic free energy models

In this appendix, we summarize the derivations of the grand-potential densities and model equations from the dilute solution model and the parabolic free energy. This derivation has been shown for a binary system by Plapp [40] and for a multicomponent multiphase system by Aagesen et al. [39].

To obtain the grand-potential densities for our model, we apply the Legendre transformation (Eq. (9)) to the free energy density. The atomic fraction is calculated using Eq. (3), which yields the relationship between the chemical potential and the atomic fraction. Since the atomic fraction and the number density are related by the atomic volume (Eq. (2)), we can derive the number density in terms of the chemical potential. Finally, the susceptibility is the derivative of the number density with respect to the chemical potential, i.e. $\chi_i \equiv \partial \rho_i / \partial \mu_i$ [40], and is used in the next section to define the evolution of the chemical potential.

The grand-potential density in the fiber phase f becomes

$$\omega^f = f_{min}^f - \frac{\mu_C}{V_a} - \frac{k_B T}{V_a} \left[\exp\left(\frac{-\mu_C - E_v^f}{k_B T}\right) + \exp\left(\frac{\mu_O - E_O^f}{k_B T}\right) + \exp\left(\frac{\mu_{CO} - E_{CO}^f}{k_B T}\right) \right]. \quad (\text{A.1})$$

The number densities of each species (C, O, and CO) are

$$\rho_C^f = -\frac{\partial \omega^f}{\partial \mu_C} = \frac{1}{V_a} \left[1 - \exp\left(\frac{-\mu_C - E_v^f}{k_B T}\right) \right], \quad (\text{A.2})$$

$$\rho_O^f = -\frac{\partial \omega^f}{\partial \mu_O} = \frac{1}{V_a} \exp\left(\frac{\mu_O - E_O^f}{k_B T}\right), \quad (\text{A.3})$$

$$\rho_{CO}^f = -\frac{\partial \omega^f}{\partial \mu_{CO}} = \frac{1}{V_a} \exp\left(\frac{\mu_{CO} - E_{CO}^f}{k_B T}\right), \quad (\text{A.4})$$

and the corresponding susceptibilities are

$$\chi_C^f = \frac{\partial \rho_C^f}{\partial \mu_C} = \frac{1}{k_B T V_a} \exp\left(\frac{-\mu_C - E_C^f}{k_B T}\right), \quad (\text{A.5})$$

$$\chi_O^f = \frac{\partial \rho_O^f}{\partial \mu_O} = \frac{1}{k_B T V_a} \exp\left(\frac{\mu_O - E_O^f}{k_B T}\right), \quad (\text{A.6})$$

$$\chi_{CO}^f = \frac{\partial \rho_{CO}^f}{\partial \mu_{CO}} = \frac{1}{k_B T V_a} \exp\left(\frac{\mu_{CO} - E_{CO}^f}{k_B T}\right). \quad (\text{A.7})$$

The grand-potential density in the gas phase g becomes

$$\omega^g = f_{min}^g - \frac{1}{2} \frac{\mu_C^2}{V_a^2 A_C^g} - \frac{\mu_C}{V_a} x_C^{g,eq} - \frac{1}{2} \frac{\mu_O^2}{V_a^2 A_O^g} - \frac{\mu_C}{V_a} x_O^{g,eq} - \frac{1}{2} \frac{\mu_{CO}^2}{V_a^2 A_{CO}^g} - \frac{\mu_{CO}}{V_a} x_{CO}^{g,eq}. \quad (\text{A.8})$$

The number density and susceptibility of each species ($i = C, O,$ and CO) become

$$\rho_i^g = -\frac{\partial \omega_g}{\partial \mu_i} = \frac{\mu_i}{V_a^2 A_i^g} + \frac{x_i^{g,eq}}{V_a}, \quad (\text{A.9})$$

$$\chi_i^g = \frac{\partial \rho_i^g}{\partial \mu_i} = \frac{1}{V_a^2 A_i^g}. \quad (\text{A.10})$$

Appendix B. Analytical model derivation

Here, we derive our analytical model for the surface oxidation of the 1D carbon fiber with a diffuse surface. The 1D domain has a length of $2s_0$. The carbon fiber is on the left of the domain and the open gaseous region is on the right. We assume that there is an infinite source of C on the left boundary and that the diffusion of C from the boundary to the fiber surface is very fast, such that the carbon fiber does not change during oxidation. The right boundary is closed and there is a finite amount of O in the system that will be consumed during oxidation. We also assume that the transport of the gaseous species is very fast.

We assume that the atomic fraction of C and O follow hyperbolic tangent profiles of the form

$$x_C(s) = \frac{1}{2} \left[1 - \tanh \left(\frac{2(s-s_0)}{\delta_x} \right) \right], \quad (\text{B.1})$$

$$x_O(s) = \frac{x_O^g}{2} \left[1 + \tanh \left(\frac{2(s-s_0)}{\delta_x} \right) \right], \quad (\text{B.2})$$

where x_O^g is the atomic fraction of O in the gaseous region, s is the position variable in the 1D domain, and δ_x is the interfacial width of the atomic fractions. $x_C = 1$ in the fiber and 0 in the gaseous region; $x_O = 0$ in the fiber and x_O^g in the gaseous region. Note that $\delta_x = b\delta_{int}$, where $b < 1$, since δ_{int} from the phase-field model defines the interface width of the order parameter profiles while δ_x defines the interface width of the atomic fraction profiles. For the switching function we use in our model (Eq. (10)), $b = 0.5$.

Because we assume that the fiber does not change during oxidation, the x_C profile does not change and the interface center does not move. Moreover, because we assume that the diffusion of the gaseous species is fast, the atomic fraction gradients within the gaseous region are zero. The atomic fraction of oxygen in the gas, x_O^g , is uniform throughout the gas phase and dictates the total amount of oxygen in the system. Fig. B.9 shows an example of profiles of the atomic fractions of C and O according to Eqs. (B.1) and (B.2) in a $10 \mu\text{m}$ 1D domain for two different interface widths. The quantity $x_C x_O > 0$ in the surface region in which the atomic fractions of the reactants are non-zero and chemical reactions may occur.

Because the O atomic fraction has no gradient within the gaseous phase, there is no diffusion and the change in the atomic fraction is defined by Eq. (21). Using the relationship of the number density and the atomic fraction from Eq. (2), we can rewrite the evolution of the atomic fraction of oxygen in the gas phase as

$$\frac{dx_O}{dt} = -\frac{\tilde{K}}{V_a} x_C x_O. \quad (\text{B.3})$$

To simplify our derivations, we combine \tilde{K} and V_a and assume that the reaction rate constant has units of $1/s$. The total amount of oxygen in the system

$$N_O = \rho_{sites} \int x_O ds, \quad (\text{B.4})$$

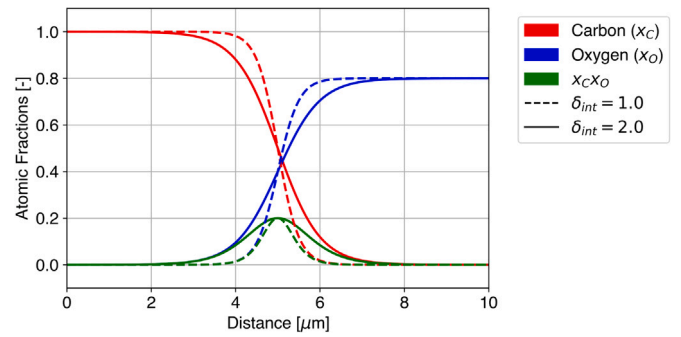


Fig. B.9. C and O atom fraction profiles assumed for the 1D analytical model of surface oxidation, as defined in Eqs. (B.1) and (B.2). The solid lines are plotted with $x_O^g = 0.8$, $\delta_x = 2 \mu\text{m}$, and $s_0 = 5 \mu\text{m}$. The product $x_C x_O$ is also shown in green, which represents the surface region where chemical reactions occur. The dashed lines represent the atomic fraction profiles for a thinner diffuse interface width $\delta_x = 1 \mu\text{m}$. The reaction area for the thinner interface width is smaller than the original area, which means that less material will be removed in a same amount of time if the reaction rate constant is not normalized.

where ρ_{sites} is the number density of sites. In 3D, the density of sites is simply the inverse of the atomic volume. To adjust this value for 1D, we assume that each atom in our lattice is in the center of a cube with side length l_a , where the value of l_a is equal to $\sqrt[3]{V_a}$. Therefore, the 1D density of sites becomes $1/l_a$ in units of atom/m, such that

$$N_O = \frac{1}{l_a} \int x_O ds, \quad (\text{B.5})$$

Recalling that the generalized diffusion equation conserves mass, and the boundaries are closed, we can describe the total change in oxygen by integrating Eq. (B.3) over the domain,

$$\int \frac{dx_O}{dt} ds = - \int \tilde{K} x_C x_O ds. \quad (\text{B.6})$$

Substituting in the atomic fraction profiles from Eqs. (B.1) and (B.2), we obtain

$$\int \frac{d}{dt} \left(\frac{x_O^g}{2} \left[1 + \tanh \left(\frac{2(s-s_0)}{\delta_x} \right) \right] \right) ds = - \int \tilde{K} \left(\frac{1}{2} \left[1 - \tanh \left(\frac{2(s-s_0)}{\delta_x} \right) \right] \right) \left(\frac{x_O^g}{2} \left[1 + \tanh \left(\frac{2(s-s_0)}{\delta_x} \right) \right] \right) ds. \quad (\text{B.7})$$

x_O^g is the only quantity that changes with time, so we pull the time derivative out of the integral on the left-hand side of Eq. (B.7) to obtain a complete formulation of the time derivative of the atomic fraction of oxygen in the gas phase,

$$\frac{dx_O^g}{dt} \int \frac{1}{2} \left[1 + \tanh \left(\frac{2(s-s_0)}{\delta_x} \right) \right] ds = - \tilde{K} x_O^g \int \frac{1}{2} \left[1 - \tanh \left(\frac{2(s-s_0)}{\delta_x} \right) \right] \frac{1}{2} \left[1 + \tanh \left(\frac{2(s-s_0)}{\delta_x} \right) \right] ds. \quad (\text{B.8})$$

Our objective is to solve Eq. (B.8) for x_O^g , which is a function of time. We can define a constant A_s to simplify Eq. (B.8),

$$A_s = \frac{\int \frac{1}{2} \left[1 - \tanh \left(\frac{2(s-s_0)}{\delta_x} \right) \right] \frac{1}{2} \left[1 + \tanh \left(\frac{2(s-s_0)}{\delta_x} \right) \right] ds}{\int \frac{1}{2} \left[1 + \tanh \left(\frac{2(s-s_0)}{\delta_x} \right) \right] ds}. \quad (\text{B.9})$$

The factor A_s (Eq. (B.9)) can be solved analytically and simplified even further. We start by simplifying the numerator to get

$$A_s = \frac{\int \frac{1}{4} \left[1 - \tanh^2 \left(\frac{2(s-s_0)}{\delta_x} \right) \right] ds}{\int \frac{1}{2} \left[1 + \tanh \left(\frac{2(s-s_0)}{\delta_x} \right) \right] ds}. \quad (\text{B.10})$$

To solve the numerator integral of Eq. (B.10), we assume that the center of the interface is at $s = 0$, and integrating from $-s_0$ to s_0 we obtain

$$\int_{-s_0}^{s_0} \frac{1}{4} \left[1 - \tanh^2 \left(\frac{2s}{\delta_x} \right) \right] ds = \frac{\delta_x}{4} \tanh \left(\frac{2s_0}{\delta_x} \right). \quad (\text{B.11})$$

If the domain size is much larger than the interface width, i.e. $2s_0 \gg \delta_x$, Eq. (B.11) can be simplified further to $\frac{\delta_x}{4}$. The denominator integral of Eq. (B.10) can be simplified in a similar manner; if $2s_0 \gg \delta_x$,

$$\int_{-s_0}^{s_0} \frac{1}{2} \left[1 + \tanh \left(\frac{2s}{\delta_x} \right) \right] ds = s_0. \quad (\text{B.12})$$

The constant A_s can be now rewritten by substituting Eqs. (B.11) and (B.12) into Eq. (B.10) to obtain

$$A_s = \frac{\delta_x}{4s_0}. \quad (\text{B.13})$$

By substituting Eq. (B.13) into Eq. (B.8), we obtain a simplified expression for the time derivative of the oxygen atomic fraction

$$\frac{dx_O^g}{dt} = -\frac{\delta_x}{4s_0} \tilde{K} x_O^g. \quad (\text{B.14})$$

The integration of Eq. (B.14) yields the time evolution of the atomic fraction of oxygen in the gas phase

$$x_O^g = x_O^{g,0} \exp \left(-\frac{\delta_x}{4s_0} \tilde{K} t \right), \quad (\text{B.15})$$

where $x_O^{g,0}$ is the initial fraction of oxygen in the gas phase.

With an expression for x_O^g , we can now obtain a value for total amount of oxygen in the system with time. By substituting Eqs. (B.2) and (B.15) into Eq. (B.5), we obtain

$$N_O(t) = \frac{1}{l_a} x_O^{g,0} \exp \left(-\frac{\delta_x}{4s_0} \tilde{K} t \right) \int_{-s_0}^{s_0} \frac{1}{2} \left[1 + \tanh \left(\frac{2(s-s_0)}{\delta_x} \right) \right] ds. \quad (\text{B.16})$$

The spatial integral in Eq. (B.16) is identical to the one in Eq. (B.12) and can be solved under the same assumptions. We finally arrive at an analytical equation that predicts the time evolution of the total amount of oxygen atoms due to the surface reaction in a 1D system with a half volume of reactant solid and gas:

$$N_O(t) = \frac{1}{l_a} s_0 x_O^{g,0} \exp \left(-\frac{\delta_x}{4s_0} \tilde{K} t \right). \quad (\text{B.17})$$

The influence of the interface width on the oxygen consumption is clear in Eq. (31). When $\tilde{K} = K/\delta_x$, this dependence on δ_x drops out.

References

- [1] H.K. Tran, Phenolic Impregnated Carbon Ablators (PICA) as Thermal Protection Systems for Discovery Missions, Tech. Rep. April, NASA Ames Research Center, 1997.
- [2] M. Stackpoole, S. Sepka, I. Cozmuta, D. Kontinos, Post-flight evaluation of stardust sample return capsule forebody heatshield material, in: 46th AIAA Aerospace Sciences Meeting and Exhibit, 2008, pp. 1–7, <http://dx.doi.org/10.2514/6.2008-1202>, URL <http://arc.aiaa.org/doi/10.2514/6.2008-1202>.
- [3] M. Natali, J.M. Kenny, L. Torre, Science and technology of polymeric ablative materials for thermal protection systems and propulsion devices: A review, Prog. Mater. Sci. 84 (2016) 192–275, <http://dx.doi.org/10.1016/j.pmatsci.2016.08.003>.
- [4] B.K. Bessire, S.A. Lahankar, T.K. Minton, Pyrolysis of phenolic impregnated carbon ablator (PICA), ACS Appl. Mater. Interfaces 7 (3) (2015) 1383–1395, <http://dx.doi.org/10.1021/am507816f>.
- [5] H.K. Tran, C.E. Johnson, D.J. Rasky, F.C. Hui, M.T. Hsu, Y.K. Chen, Phenolic impregnated carbon ablators (PICA) for discovery class missions, in: 31st Thermophysics Conference, 1996, <http://dx.doi.org/10.2514/6.1996-1911>, URL <https://arc.aiaa.org/doi/abs/10.2514/6.1996-1911>.
- [6] R. Jambunathan, D.A. Levin, A. Borner, J.C. Ferguson, F. Panerai, Prediction of gas transport properties through fibrous carbon preform microstructures using Direct Simulation Monte Carlo, Int. J. Heat Mass Transfer 130 (2019) 923–937, <http://dx.doi.org/10.1016/j.ijheatmasstransfer.2018.11.006>.
- [7] P. Agrawal, J.F. Chavez-Garcia, Fracture in phenolic impregnated carbon ablator, in: 42nd AIAA Thermophysics Conference, 2011, pp. 1–12, <http://dx.doi.org/10.2514/6.2011-3492>.

- [8] M. Natali, I. Puri, J.M. Kenny, L. Torre, M. Rallini, Microstructure and ablation behavior of an affordable and reliable nanostructured Phenolic Impregnated Carbon Ablator (PICA), Polym. Degrad. Stab. 141 (2017) 84–96, <http://dx.doi.org/10.1016/j.polymdegradstab.2017.05.017>.
- [9] M. Stackpoole, E. Venkatapathy, S. Violette, Sustaining PICA for future NASA robotic science missions including NF-4 and discovery, in: IEEE Aerospace Conference Proceedings, Vol. 2018-March, 2018, pp. 1–7, <http://dx.doi.org/10.1109/AERO.2018.8396774>.
- [10] M. Inagaki, N. Iwashita, Y. Hishiyama, Y. Kaburagi, A. Yoshida, A. Oberlin, K. Lafdi, S. Bonnamy, Y. Yamada, Studies on "Mesophase"-pitch-based carbon fibers: Part I structure and textures, TANSO 147 (1991) 57–65.
- [11] S. Desai, C. Li, T. Shen, A. Strachan, Molecular modeling of the microstructure evolution during carbon fiber processing, J. Chem. Phys. 147 (22) (2017) 224705, <http://dx.doi.org/10.1063/1.5000911>.
- [12] L. Shi, M. Sessim, M.R. Tonks, S.R. Phillpot, Generation and characterization of an improved carbon fiber model by molecular dynamics, Carbon 173 (2021) 232–244, <http://dx.doi.org/10.1016/j.carbon.2020.11.011>.
- [13] C. Ho, R.W. Powell, P.E. Liley, Thermal conductivity of the elements, J. Phys. Chem. Ref. Data 1 (2) (1972) 279, <http://dx.doi.org/10.1016/B978-0-444-53802-4.00047-6>, URL <https://doi.org/10.1063/1.3253100>.
- [14] C.Y. Ho, R.W. Powell, P.E. Liley, Thermal conductivity of the elements: A comprehensive review, J. Phys. Chem. Ref. Data 3 (1) (1974) 1–756, <http://dx.doi.org/10.1063/1.3253100>.
- [15] G. Fugallo, A. Cepellotti, L. Paulatto, M. Lazzeri, N. Marzari, F. Mauri, Thermal conductivity of graphene and graphite: Collective excitations and mean free paths, Nano Lett. 14 (11) (2014) 6109–6114, <http://dx.doi.org/10.1021/nl502059f>.
- [16] B. Nysten, J.P. Issi, R. Barton, D.R. Boyington, J.G. Lavin, Determination of lattice defects in carbon fibers by means of thermal-conductivity measurements, Phys. Rev. B 44 (5) (1991) 2142–2148, <http://dx.doi.org/10.1103/PhysRevB.44.2142>.
- [17] L. Qiu, X.H. Zheng, J. Zhu, G.P. Su, D.W. Tang, The effect of grain size on the lattice thermal conductivity of an individual polyacrylonitrile-based carbon fiber, Carbon 51 (1) (2013) 265–273, <http://dx.doi.org/10.1016/j.carbon.2012.08.052>.
- [18] C. Pradere, J.C. Batsale, J.M. Goyh  n  che, R. Pailler, S. Dilhaire, Thermal properties of carbon fibers at very high temperature, Carbon 47 (3) (2009) 737–743, <http://dx.doi.org/10.1016/j.carbon.2008.11.015>.
- [19] E.G. Hughes, B. Williams, J.M. Thomas, Etching of graphite surfaces with oxygen, Trans. Faraday Soc. 58 (1962) 2011–2016, URL <http://dx.doi.org/10.1039/TF9625802011>.
- [20] S. Poovathingal, T.E. Schwartzentruber, S.G. Srinivasan, A.C.T. van Duin, Computational chemistry modelling of the oxidation of highly oriented Pyrolytic Graphite, J. Phys. Chem. A 117 (13) (2013) 2692–2703, <http://dx.doi.org/10.1021/jp3125999>.
- [21] M. Minus, S. Kumar, The processing, properties, and structure of carbon fibers, JOM 57 (2) (2005) 52–58, <http://dx.doi.org/10.1007/s11837-005-0217-8>, URL <http://link.springer.com/10.1007/s11837-005-0217-8>.
- [22] F. Panerai, J.C. Ferguson, J. Lachaud, A. Martin, M.J. Gasch, N.N. Mansour, Micro-tomography based analysis of thermal conductivity, diffusivity and oxidation behavior of rigid and flexible fibrous insulators, Int. J. Heat Mass Transfer 108 (2017) 801–811, <http://dx.doi.org/10.1016/j.ijheatmasstransfer.2016.12.048>.
- [23] Y.K. Chen, F.S. Milos, Ablation and thermal response program for spacecraft heatshield analysis, in: 36th AIAA Aerospace Sciences Meeting and Exhibit, Vol. 36, 1999, pp. 475–483, <http://dx.doi.org/10.2514/2.3469>, (3).
- [24] D. Driver, M. MacLean, Improved predictions of PICA recession in arc jet shear tests, in: 49th AIAA Aerospace Sciences Meeting Including the New Horizons Forum and Aerospace Exposition, 2011, <http://dx.doi.org/10.2514/6.2011-141>.
- [25] J. Lachaud, N.N. Mansour, Porous-material analysis toolbox based on openfoam and applications, J. Thermophys. Heat Transfer 28 (2) (2014) 191–202, <http://dx.doi.org/10.2514/1.T4262>.
- [26] J.R. Lachaud, T.E. Magin, I. Cozmuta, N.N. Mansour, A short review of ablative-material response models and simulation tools, in: 7th Aerothermodynamics Symposium, 2011, URL <https://ntrs.nasa.gov/api/citations/201110014340/downloads/20110014340.pdf>.
- [27] H. Weng, A. Martin, Multidimensional modeling of pyrolysis gas transport inside charring ablative materials, J. Thermophys. Heat Transfer 28 (4) (2014) 583–597, <http://dx.doi.org/10.2514/1.T4434>, URL <http://arc.aiaa.org/doi/10.2514/1.T4434>.
- [28] J. Lachaud, G.L. Vignoles, A Brownian motion technique to simulate gasification and its application to C/C composite ablation, Comput. Mater. Sci. 44 (4) (2009) 1034–1041, <http://dx.doi.org/10.1016/j.commatsci.2008.07.015>.
- [29] J.C. Ferguson, F. Panerai, J. Lachaud, A. Martin, S.C. Bailey, N.N. Mansour, Modeling the oxidation of low-density carbon fiber material based on micro-tomography, Carbon 96 (2016) 57–65, <http://dx.doi.org/10.1016/j.carbon.2015.08.113>.
- [30] J. Lachaud, Y. Aspa, G.L. Vignoles, Analytical modeling of the transient ablation of a 3D C/C composite, Int. J. Heat Mass Transfer 115 (2017) 1150–1165, <http://dx.doi.org/10.1016/j.ijheatmasstransfer.2017.06.130>.
- [31] J. Lachaud, I. Cozmuta, N.N. Mansour, Multiscale approach to ablation modeling of phenolic impregnated carbon ablators, J. Spacecr. Rockets 47 (6) (2010) 910–921, <http://dx.doi.org/10.2514/1.42681>.

- [32] L.-Q.Q. Chen, Phase-field models for microstructure evolution, *Annu. Rev. Mater. Sci.* 32 (1) (2002) 113–140, <http://dx.doi.org/10.1146/annurev.matsci.32.112001.132041>, URL <http://www.annualreviews.org/doi/10.1146/annurev.matsci.32.112001.132041>.
- [33] N. Moelans, B. Blanpain, P. Wollants, An introduction to phase-field modeling of microstructure evolution, *Calphad: Comput. Coupling Phase Diagr. Thermochem.* 32 (2) (2008) 268–294, <http://dx.doi.org/10.1016/j.calphad.2007.11.003>.
- [34] M.R. Tonks, L.K. Aagesen, The phase field method: Mesoscale simulation aiding material discovery, *Annu. Rev. Mater. Res.* 49 (2019) 79–102, <http://dx.doi.org/10.1146/annurev-matsci-070218-010151>.
- [35] M. Sessim, M.R. Tonks, Macaw: A mesoscale ablation modeling tool, 2021, URL <https://github.com/tonkmr/macaw>.
- [36] D. Gaston, C. Newman, G. Hansen, D. Lebrun-Grandié, MOOSE: A parallel computational framework for coupled systems of nonlinear equations, *Nucl. Eng. Des.* 239 (10) (2009) 1768–1778, <http://dx.doi.org/10.1016/j.nucengdes.2009.05.021>.
- [37] C.J. Permann, D.R. Gaston, D. Andrš, R.W. Carlsen, F. Kong, A.D. Lindsay, J.M. Miller, J.W. Peterson, A.E. Slaughter, R.H. Stogner, R.C. Martineau, MOOSE: Enabling massively parallel multiphysics simulation, *SoftwareX* 11 (2020) 100430, <http://dx.doi.org/10.1016/j.softx.2020.100430>, arXiv:1911.04488.
- [38] N. Moelans, B. Blanpain, P. Wollants, Quantitative analysis of grain boundary properties in a generalized phase field model for grain growth in anisotropic systems, *Phys. Rev. B* 78 (2) (2008) 024113, <http://dx.doi.org/10.1103/PhysRevB.78.024113>, URL <https://link.aps.org/doi/10.1103/PhysRevB.78.024113>.
- [39] L.K. Aagesen, Y. Gao, D. Schwen, K. Ahmed, Grand-potential-based phase-field model for multiple phases, grains, and chemical components, *Phys. Rev. E* 98 (2) (2018) 1–16, <http://dx.doi.org/10.1103/PhysRevE.98.023309>.
- [40] M. Plapp, Unified derivation of phase-field models for alloy solidification from a grand-potential functional, *Phys. Rev. E* 84 (3) (2011) 1–15, <http://dx.doi.org/10.1103/PhysRevE.84.031601>, arXiv:1105.1670.
- [41] I. Greenquist, M.R. Tonks, L.K. Aagesen, Y. Zhang, Development of a microstructural grand potential-based sintering model, *Comput. Mater. Sci.* 172 (August 2019) (2020) 109288, <http://dx.doi.org/10.1016/j.commatsci.2019.109288>.
- [42] P.C.A. Simon, L.K. Aagesen, A.T. Motta, M.R. Tonks, The effects of introducing elasticity using different interpolation schemes to the grand potential phase field model, *Comput. Mater. Sci.* 183 (May) (2020) 109790, <http://dx.doi.org/10.1016/j.commatsci.2020.109790>.
- [43] N. Moelans, A quantitative and thermodynamically consistent phase-field interpolation function for multi-phase systems, *Acta Mater.* 59 (3) (2011) 1077–1086, <http://dx.doi.org/10.1016/j.actamat.2010.10.038>.
- [44] J.W. Cahn, S.M. Allen, A microscopic theory for domain wall motion and its experimental verification in Fe-Al alloy domain growth kinetics, *J. Phys. Colloq.* 38 (C7) (1977) C7–51–C7–54, <http://dx.doi.org/10.1051/jphyscol:1977709>.
- [45] C. Sun, B. Bai, Gas diffusion on graphene surfaces, *Phys. Chem. Chem. Phys.* 19 (5) (2017) 3894–3902, <http://dx.doi.org/10.1039/c6cp06267a>.
- [46] C. Qiu, Y. Wang, Y. Li, X. Sun, G. Zhuang, Z. Yao, S. Deng, J. Wang, A generalized formula for two-dimensional diffusion of CO in graphene nanoslits with different Pt loadings, *Green Energy Environ.* 5 (3) (2020) 322–332, <http://dx.doi.org/10.1016/j.gjee.2020.04.012>.
- [47] S. Poovathingal, T.E. Schwartzentruber, V.J. Murray, T.K. Minton, G.V. Candler, Finite-rate oxidation model for carbon surfaces from molecular beam experiments, *AIAA J.* 55 (5) (2017) 1644–1658, <http://dx.doi.org/10.2514/1.J055371>.
- [48] K. Swaminathan-Gopalan, A. Borner, V.J. Murray, S. Poovathingal, T.K. Minton, N.N. Mansour, K.A. Stephani, Development and validation of a finite-rate model for carbon oxidation by atomic oxygen, *Carbon* 137 (2018) 313–332, <http://dx.doi.org/10.1016/j.carbon.2018.04.088>.
- [49] M. Schneider, M. Kabel, H. Andrä, A. Lenske, M. Hauptmann, J.P. Majschak, L. Penner, A. Hardtmann, S. Ihlenfeldt, R. Westerteiger, E. Glatt, A. Wiegmann, Thermal fiber orientation tensors for digital paper physics, *Int. J. Solids Struct.* 100–101 (2016) 234–244, <http://dx.doi.org/10.1016/j.ijsolstr.2016.08.020>.
- [50] B.S. Kirk, J.W. Peterson, R.H. Stogner, G.F. Carey, libMesh : a C++ library for parallel adaptive mesh refinement/coarsening simulations, *Eng. Comput.* 22 (3–4) (2006) 237–254, <http://dx.doi.org/10.1007/s00366-006-0049-3>.
- [51] S. Balay, S. Abhyankar, M.F. Adams, J. Brown, P. Brune, K. Buschelman, L. Dalcin, A. Dener, V. Eijkhout, W.D. Gropp, D. Karpeyev, D. Kaushik, M.G. Knepley, D.A. May, L.C. McInnes, R.T. Mills, T. Munson, K. Rupp, P. Sanan, B.F. Smith, S. Zampini, H. Zhang, H. Zhang, PETSc Users Manual, Tech. Rep. ANL-95/11 - Revision 3.15, Argonne National Laboratory, 2021, URL <https://www.mcs.anl.gov/petsc>.
- [52] S. Balay, W.D. Gropp, L.C. McInnes, B.F. Smith, Efficient management of parallelism in object oriented numerical software libraries, in: E. Arge, A.M. Bruaset, H.P. Langtangen (Eds.), *Modern Software Tools in Scientific Computing*, Birkhäuser Press, 1997, pp. 163–202.
- [53] V.E. Henson, U.M. Yang, BoomerAMG: A parallel algebraic multigrid solver and preconditioner, *Appl. Numer. Math.* 41 (1) (2002) 155–177, [http://dx.doi.org/10.1016/S0168-9274\(01\)00115-5](http://dx.doi.org/10.1016/S0168-9274(01)00115-5).
- [54] E.W. Lemmon, R.T. Jacobsen, Viscosity and thermal conductivity equations for nitrogen, oxygen, argon, and air, *Int. J. Thermophys.* 25 (1) (2004) 21–69.
- [55] M.A. Kanter, Diffusion of carbon atoms in natural graphite crystals, *Phys. Rev.* 107 (3) (1957) 655–663, <http://dx.doi.org/10.1103/PhysRev.107.655>.
- [56] E.L. Cussler, *Diffusion: Mass Transfer in Fluid Systems*, third ed., Cambridge University Press, 2009, p. 631.
- [57] S. Wasik, K. McCulloh, Measurements of gaseous diffusion coefficients by a gas chromatographic technique, *J. Res. Natl. Bur. Stand. A* 73A (2) (1969) 207, <http://dx.doi.org/10.6028/jres.073a.018>.
- [58] M.W. Chase, NIST-JANAF thermochemical tables, *J. Phys. Chem. Ref. Data* 9 (1998) 1.
- [59] H. Zaidi, F. Robert, D. Paulmier, Influence of adsorbed gases on the surface energy of graphite: consequences on the friction behaviour, *Thin Solid Films* 264 (1) (1995) 46–51, [http://dx.doi.org/10.1016/0040-6090\(95\)06606-3](http://dx.doi.org/10.1016/0040-6090(95)06606-3).
- [60] J. Abrahamson, The surface energies of graphite, *Carbon* 11 (4) (1973) 337–362.
- [61] C.D. Van Engers, N.E. Cousins, V. Babenko, J. Britton, B. Zappone, N. Grobert, S. Perkin, Direct measurement of the surface energy of graphene, *Nano Lett.* 17 (6) (2017) 3815–3821, <http://dx.doi.org/10.1021/acs.nanolett.7b01181>.
- [62] B. Ruscic, D. Feller, K.A. Peterson, Active thermochemical tables: Dissociation energies of several homonuclear first-row diatomics and related thermochemical values, *Theor. Chem. Acc.* 133 (1) (2014) 1–12, <http://dx.doi.org/10.1007/s00214-013-1415-z>.
- [63] L. Li, S. Reich, J. Robertson, Defect energies of graphite: Density-functional calculations, *Phys. Rev. B* 72 (18) (2005) 1–10, <http://dx.doi.org/10.1103/PhysRevB.72.184109>.
- [64] H. Zhang, M. Zhao, X. Yang, H. Xia, X. Liu, Y. Xia, Diffusion and coalescence of vacancies and interstitials in graphite: A first-principles study, *Diam. Relat. Mater.* 19 (10) (2010) 1240–1244, <http://dx.doi.org/10.1016/j.diamond.2010.06.010>.
- [65] A. El-Barbary, H. Telling, P. Ewels, I. Heggie, R. Briddon, Structure and energetics of the vacancy in graphite, *Phys. Rev. B* 68 (14) (2003) 1–7, <http://dx.doi.org/10.1103/PhysRevB.68.144107>.
- [66] F. Mehmood, R. Pachter, W. Lu, J.J. Boeckl, Adsorption and diffusion of oxygen on single-layer graphene with topological defects, *J. Phys. Chem. C* 117 (20) (2013) 10366–10374, <http://dx.doi.org/10.1021/jp312159v>.
- [67] T. Sun, S. Fabris, S. Baroni, Surface precursors and reaction mechanisms for the thermal reduction of graphene basal surfaces oxidized by atomic oxygen, *J. Phys. Chem. C* 115 (11) (2011) 4730–4737, <http://dx.doi.org/10.1021/jp111372k>.
- [68] F. Semeraro, J.C. Ferguson, F. Panerai, R.J. King, N.N. Mansour, Anisotropic analysis of fibrous and woven materials part I: Estimation of local orientation, *Comput. Mater. Sci.* 178 (February) (2020) 109631, <http://dx.doi.org/10.1016/j.commatsci.2020.109631>.
- [69] B.M. Adams, M.S. Eldred, G. Geraci, R.W. Hooper, J.D. Jakeman, K.A. Maupin, J.A. Monschke, A.A. Rushdi, J.A. Stephens, L.P. Swiler, T.M. Wildey, Dakota, A Multilevel Parallel Object-Oriented Framework for Design Optimization, Parameter Estimation, Uncertainty Quantification, and Sensitivity Analysis: Version 6.10 User's Manual Brian, Tech. rep., Sandia Technical Report SAND2014-4633, Sandia National Laboratories, 2014, URL <http://linkinghub.elsevier.com/retrieve/pii/S0951832005002437>.
- [70] F. Panerai, T. Cochell, A. Martin, J.D. White, Experimental measurements of the high-temperature oxidation of carbon fibers, *Int. J. Heat Mass Transfer* 136 (2019) 972–986, <http://dx.doi.org/10.1016/j.ijheatmasstransfer.2019.03.018>.
- [71] J.B.E. Meurisse, J. Lachaud, F. Panerai, C. Tang, N.N. Mansour, Multidimensional material response simulations of a full-scale tiled ablative heatshield, *Aerosp. Sci. Technol.* 76 (2018) 497–511, <http://dx.doi.org/10.1016/j.ast.2018.01.013>.